Marine Micropaleontology 191 (2024) 102395

Contents lists available at ScienceDirect

Marine Micropaleontology

journal homepage: www.elsevier.com/locate/marmicro

Unravelling changes in the productivity regime during the Late Miocene-Early Pliocene Biogenic Bloom: Insights from the western equatorial Pacific (IODP Site U1488)

Maria Elena Gastaldello[a,b,*], Claudia Agnini[a], Thomas Westerhold[c], Anna Joy Drury[d,e], Laia Alegret[b,f]

[a] Dipartimento di Geoscienze, Università Degli Studi di Padova, Padova, Italy
[b] Departamento de Ciencias de la Tierra, Universidad de Zaragoza, Spain
[c] MARUM - Center for Marine Environmental Sciences, University of Bremen, Germany
[d] School of Geography, Geology and the Environment, University of Leicester, Leicester, UK
[e] Department of Earth Sciences, University College London, London, UK
[f] Instituto de Investigación en Ciencias Ambientales de Aragón, Universidad de Zaragoza, Spain

ARTICLE INFO

Keywords:
Late Miocene
Early Pliocene
Biogenic Bloom
IODP Site U1488
Benthic foraminifera

ABSTRACT

The Late Miocene-Early Pliocene Biogenic Bloom (9.0–3.5 Ma) is a widespread paleoceanographic phenomenon marked by increased marine biological productivity and by high accumulations of biological components documented at multiple open ocean sites in the Indian, Pacific, and Atlantic oceans. We investigate the expression of the Biogenic Bloom at International Ocean Discovery Program (IODP) Site U1488 in the western equatorial Pacific Ocean. We generated an improved age model based on calcareous nannofossil biostratigraphy and a quantitative benthic foraminiferal record across the Late Miocene to the Early Pliocene. Increased carbonate mass accumulation rates suggest the Biogenic Bloom occurs between 8.1 and 4.0 Ma at Site U1488. We described four intervals with paleoenvironmental significance: Interval 1 (8.1–6.2 Ma), Interval 2 (6.2–5.5 Ma), Interval 3 (5.5–4.5 Ma), and Interval 4 (4.5–3.1 Ma), the Biogenic Bloom spans across Interval 1 and 3. Intervals 1, 3, and 4 are marked by high abundance of phytodetritus exploiting taxa, related to phases of El Niño-like conditions. The highest abundance of these species during Interval 1 has been related to a phase of higher seasonality. In contrast, intervals 3 and 4 show reduced seasonality and a steadier input of food to the seafloor, associated with increased dust supply through wind transport and/or increased continental weathering during the Pliocene. Interval 2 stands out as the sole interval encompassing La Niña-like conditions, marked by a shift in the nutrient composition reaching the seafloor, from labile phytodetritus to refractory organic matter, and possibly a decrease in seasonality.

1. Introduction

The Late Miocene-Early Pliocene Biogenic Bloom (ca. 9.0–3.5 Ma; referred to as Biogenic Bloom from now on) is a paleoceanographic phenomenon marked by increased marine biological productivity. Described for the first time in the eastern equatorial Pacific (EEP) by Farrell et al. (1995), over the years this phenomenon has been recognised globally, from the Atlantic Ocean (Hermoyian and Owen, 2001; Diester-Haass et al., 2005; Drury et al., 2021; Gastaldello et al., 2024b), to the Indian Ocean (Peterson et al., 1992; Dickens and Owen, 1999), and the Pacific Ocean (Berger et al., 1993; Grant and Dickens, 2002; Lyle et al., 2019; Reghellin et al., 2022; Gastaldello et al., 2023). An increase in the accumulation of the inorganic biological components, such as $CaCO_3$ and SiO_2 is often used as to identify the Biogenic Bloom in marine sediments (Farrell et al., 1995; Dickens and Owen, 1999; Hermoyian and Owen, 2001; Grant and Dickens, 2002; Diester-Haass et al., 2005; Lyle et al., 2019). However, accumulation rate data reveals little about the exact source of the biogenic matter, and can additionally be impacted by post-depositional changes. Other lines of evidence include the presence of high productivity diatom assemblages (e.g., Mikkelsen, 1990; Dickens and Barron, 1997), the high abundance of suboxic and dysoxic benthic foraminifera (specifically *Uvigerina* spp. and buliminids s.l.), and

---

[*] Corresponding author at: Dipartimento di Geoscienze, Università Degli Studi di Padova, Padova, Italy.
E-mail address: mariaelena.gastaldello@phd.unipd.it (M.E. Gastaldello).

https://doi.org/10.1016/j.marmicro.2024.102395
Received 10 May 2024; Received in revised form 14 August 2024; Accepted 26 August 2024

changes in sediment geochemistry (e.g., reduced Mn/Sc ratio). These records reveal more about the type of productivity, with the last two suggesting low dissolved oxygen at intermediate water depths (Dickens and Owen, 1994; Farrell et al., 1995; Nomura et al., 1991; Gupta and Thomas, 1999; Lyle et al., 2019). Despite numerous studies available on various aspects of this long-lasting event, a comprehensive explanation of the exact mechanisms triggering the Biogenic Bloom is still in progress. Two complementary hypotheses have been proposed. The first invokes an increase in weathering, and the subsequently increase in nutrient supply to the global ocean (e.g., Filippelli, 1997; Dickens and Owen, 1999; Hermoyian and Owen, 2001). The second one is related to the redistribution of nutrients within the oceans due to a reorganization of oceanic circulation (Farrell et al., 1995; Dickens and Owen, 1999; Diester-Haass et al., 2002).

Further complexity comes from the regional expressions and possible diachroneity of the Biogenic Bloom. Determining the timing of the Biogenic Bloom at a global scale currently poses a challenging task. The majority of previous studies on the Biogenic Bloom that utilize datasets characterised by low resolution and/or imprecise age models, suggest a scenario in which the onset and conclusion of the Biogenic Bloom are significantly diachronous (e.g., Dickens and Owen, 1999; Hermoyian and Owen, 2001; Grant and Dickens, 2002; Pillot et al., 2023 and references therein). In contrast, recent high-resolution records with astronomically-tuned age models point to a synchronous onset at around 8.0 Ma and a diachronous end of the event, particularly between the Atlantic and the Pacific oceans (Lyle et al., 2019; Drury et al., 2021; Gastaldello et al., 2023). Records in the Atlantic Ocean indicate a more extended event, persisting until approximately 3.0 Ma (Drury et al., 2021; Pillot et al., 2023; Gastaldello et al., 2024b), whereas the Biogenic Bloom ended in the Pacific Ocean at around 4.6–4.4 Ma (Lyle et al., 2019; Gastaldello et al., 2023), seemingly mirrored in the wider low-latitudes (Karatsolis et al., 2022). Establishing a robust chronological framework is therefore essential to investigate the dynamics of the Biogenic Bloom, and to compare different datasets distributed worldwide. The opportunity to compare data perfectly aligned chronologically would allow for a thoughtful discussion on how and to what extent local signals may obscure the global signal of anomalous high productivity, which is the fingerprint of the Biogenic Bloom.

There are two fundamental questions to advance the discussion on the Biogenic Bloom. Firstly, it is necessary to understand whether this multimillion-year event has a globally synchronous onset and ending. This point is crucial to identify potential triggering mechanisms: if the onset and end of the Biogenic Bloom are synchronous, global trigger mechanisms are more likely; conversely, if the onset and end are diachronous, local mechanisms and processes may have a significant influence. In this sense, having the largest possible number of datasets from different settings and with precise age models would allow us to address this first question. The second question pertains to the impossibility of maintaining elevated productivity conditions for several million years. In this regard, the comparison of paleoenvironmental and paleoceanographic proxies based on benthic foraminifera indicates that we should view the Biogenic Bloom as a complex combination of different productivity regimes instead of solely an interval of stable high productivity conditions (e.g., Gastaldello et al., 2023, 2024b). This more complex and nuanced view could go a long way towards reconciling the apparent inconsistencies in the Biogenic Bloom onset and termination.

Here, we aim to address these two fundamental questions concerning the Biogenic Bloom in the western equatorial Pacific (WEP). While numerous studies have focused on the Biogenic Bloom in the EEP (e.g., Farrell et al., 1995; Lyle and Baldauf, 2015; Drury et al., 2018; Lyle et al., 2019; Reghellin et al., 2022), the WEP has been comparatively understudied. We address this gap by analysing the Late Miocene-Early Pliocene interval (8.1–3.1 Ma) at International Ocean Discovery Program (IODP) Site U1488, located centrally in the WEP. Firstly, we constructed a refined age model for Site U1488 based on calcareous nannofossil biostratigraphy and use the improved age control to calculate carbonate mass accumulation rates and identify the Biogenic Bloom in the WEP. Secondly, we perform quantitative and statistical analysis of benthic foraminiferal assemblages to infer the paleoceanographic changes at Site U1488, with a particular focus on changes in bottom ocean conditions. This will crucially allow us to identify any changes in local productivity regime in the WEP during the Biogenic Bloom.

2. Materials and methods

2.1. IODP Site U1488: location and study material

IODP Site U1488 (02°02.59′N, 141°45.29′E; 2604 m water depth) was drilled in the western equatorial Pacific Ocean. The site is located in the southern part of the Eauripik Rise, within Caroline Basin north of Papua New Guinea (Rosenthal et al., 2018). This location falls within the Western Pacific Warm Pool (WPWP), recognised as the largest singular expanse of warm water globally, playing a fundamental role in the overall climate dynamics (Siedler et al., 2004).

Sediments recovered from Site U1488 are described as one single lithological unit that spans the Upper Miocene to Recent, and consists of foraminifer-nannofossil ooze with a minor component of siliciclastic and volcanogenic sediments. (Rosenthal et al., 2018). Three holes were cored at Site U1448 (Holes U1488A, U1488B and U1488C; Rosenthal et al., 2018), which could be combined to form a complete succession. We use the revised composite depth scale (Revised CCSF, from here on referred to as m; Drury et al., 2021). Our study focuses on a 210-m-thick interval of foraminifera-nannofossil ooze spanning the revised composite splice (Drury et al., 2021) between Core 9H to Core 30H of Holes U1488A, U1488B, and U1488C (85.02 to 297.86 m). This interval spans from the Late Miocene to Early Pliocene (Rosenthal et al., 2018).

2.2. Modern oceanographic setting

During the Late Miocene to Early Pliocene, surface circulation in the equatorial Pacific Ocean displayed features broadly similar to its modern counterpart (Kennett et al., 1986; Savin et al., 1985; Gasperi and Kennett, 1993). The WEP is influenced by a complex system of surface and subsurface currents (Fig. 1). Surface circulation above Site U1488 is influenced by the New Guinea Coastal Current (NGCC), the westward South Equatorial Current (SEC), and the eastward North Equatorial Countercurrent (NECC; Fig. 1a). In the subsurface (Fig. 1a), the New Guinea Coastal Undercurrent (NGCUC) transports high-salinity waters and travels north along the coast of New Guinea before turning east at ca. 143°E and becoming into the Equatorial Undercurrent (EUC), also known as the Cromwell Current (Toole et al., 1988; Tsuchiya et al., 1989; Fine et al., 1994; Hu et al., 2015). The EUC is enriched in particulate iron, aluminium and manganese (Coale et al., 1996; Gordon et al., 1997). Due to its location, Site U1488 is sensitive to the Western Pacific Warm Pool (WPWP), which is in turn impacted by the El Niño-Southern Oscillation (ENSO). Beneath the EUC, the Equatorial Intermediate Current (EIC; 300 to 500 m water depth), an intermediate current located between 3°N and 2°S, flows westward and is bordered by the North and South Subsurface Countercurrents (NSCC and SSCC) (Firing, 1987; Lacan and Jeandel, 2001; Johnson et al., 2002; Gouriou et al., 2006).

At intermediate depths (Fig. 1b), the Antarctic Intermediate Water (AAIW) flows from southern high latitudes northward, crossing the Tasman Sea, the Coral Sea and the Solomon Sea, finally reaching the Bismarck Sea through the Vitiaz Strait (Tsuchiya, 1991; Kaneko et al., 1998). The circulation between 500 and 1500 m along the equatorial Pacific Ocean is complex and presents symmetric cyclonic gyres (Reid, 1997). Between 600 and 1200 m water depths, beneath the NSCC, the North Intermediate Countercurrent (NICC) flows eastward and it is the northern boundary of the westward Lower Equatorial Intermediate Current (L-EIC) (Cravatte et al., 2017; Marin et al., 2010). At greater depths (Fig. 1b), the Upper Circumpolar Deep Water (UCDW;

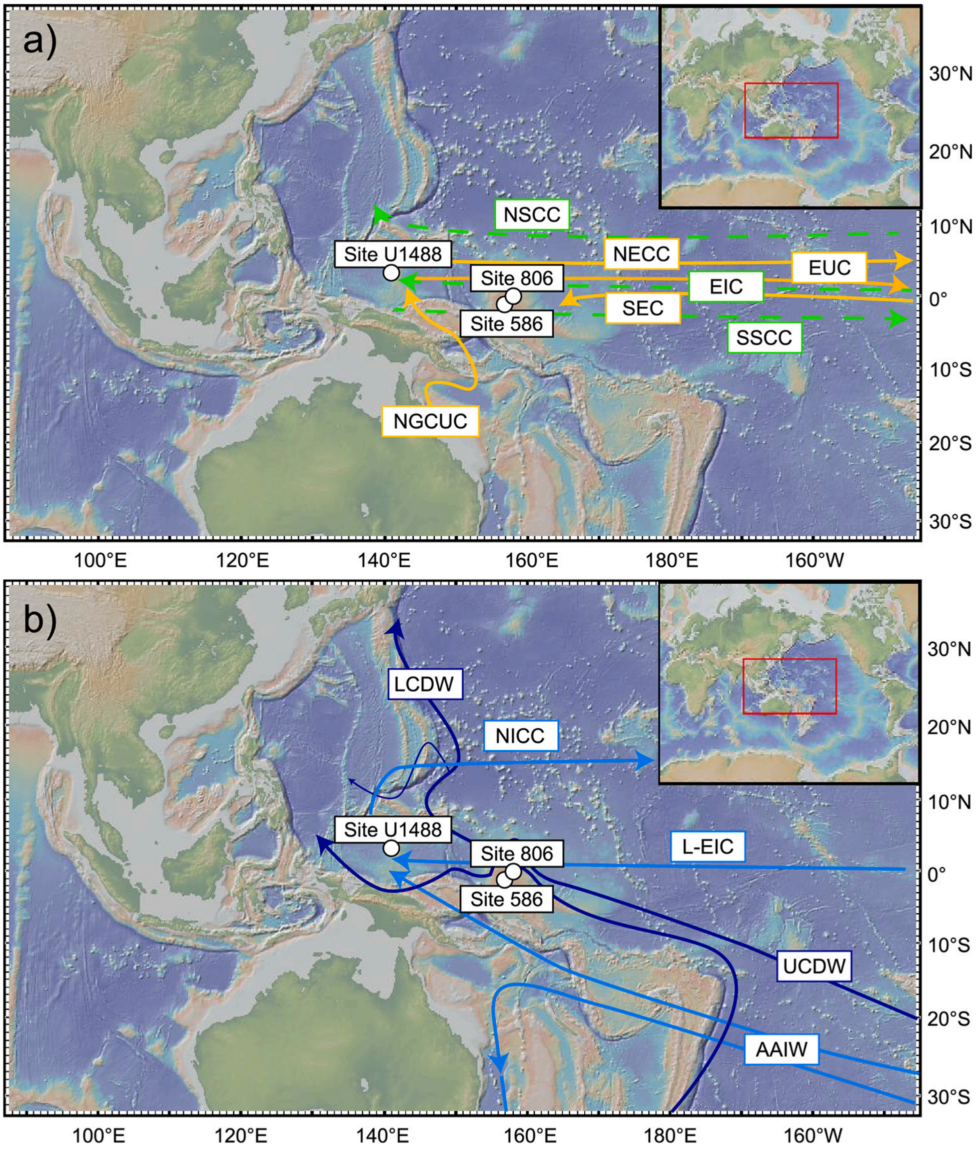

Fig. 1. Location map of IODP Site U1488 (red dot), Ocean Drilling Program (ODP) Site 806 (Resig and Cheong, 1997), and Deep Sea Drilling Program (DSDP) Site 586 (Hermelin, 1989). Figure made with GeoMapApp (http://www.geomapapp.org, last access:03/01/2024). Circulation patterns in the equatorial Pacific Ocean: a) surface (orange arrows) currents, New Guinea Coastal Current (NGCUC), South Equatorial Current (SEC), North Equatorial Countercurrent (NECC), Equatorial Undercurrent (EUC), and subsurface currents (green dotted arrows), Equatorial Intermediate Current (EIC), and North and South Subsurface Countercurrents (NSCC and SSCC) (Firing, 1987; Lacan and Jeandel, 2001; Johnson et al., 2002; Gouriou et al., 2006); b) intermediate waters (light blue arrows), Antarctic Intermediate Water (AAIW), North Intermediate Countercurrents (NICC), Lower Equatorial Intermediate Current (L-EIC) (Tsuchiya, 1991; Kaneko et al., 1998; Marin et al., 2010; Cravatte et al., 2017), and deep waters (dark blue arrows), Upper Circumpolar Deep Water (UCDW) and Lower Circumpolar Deep Water (LCDW) (Reid, 1997; Kawabe et al., 2003: Johnson, 2008; Kawabe and Fujio, 2010). (For interpretation of the references to colour in this figure legend, the reader is referred to the web version of this article.)

1500–2500 m water depth) and the Lower Circumpolar Water (LCPW; >2500 m water depth) flow into the Central Pacific through the Samoan Passage at ca. 10°S (Kawabe et al., 2003: Kawabe and Fujio, 2010; Tian et al., 2021). The UCDW reaching the Caroline Basin is characterised by low oxygen levels (Reid, 1997; Kawabe and Fujio, 2010), while the LCPW is marked by high salinity, a positive oxygen anomaly, and a minimum of silica (Kawabe et al., 2003; Johnson, 2008; Kawabe and Fujio, 2010).

2.3. Calcareous nannofossils

Between 297.86 and 85.02 m, a total of 33 samples were prepared using the standard "smear slide" method (Bown and Young, 1998). The average sample resolution is 6.5 m, which corresponds to ca. 170 kyr resolution (Suppl. Material S1). Calcareous nannofossil analyses were performed to assess the semi-quantitative abundance of selected taxa present in the fossil assemblages. Samples were examined using a Zeiss light microscope at 1250× magnification at both parallel and crossing nicols.

Due to the scarcity of some marker species, counting 300 specimens does not ensure the common and continuous detection of various taxa. For this reason, it was preferred to use a routinely employed biostratigraphic counting method that focuses solely on the taxa of interest, tallying the number of specimens of marker species in a predetermined area of 1 mm^2 (Backman and Shackleton, 1983). This approach results in more reliable abundance patterns. We use the terminology proposed by Agnini et al. (2014) for biostratigraphic events (Fig. 2; Table 1): Base (B), Base Common (Bc), Top (T), and Top Common (Tc). We additionally

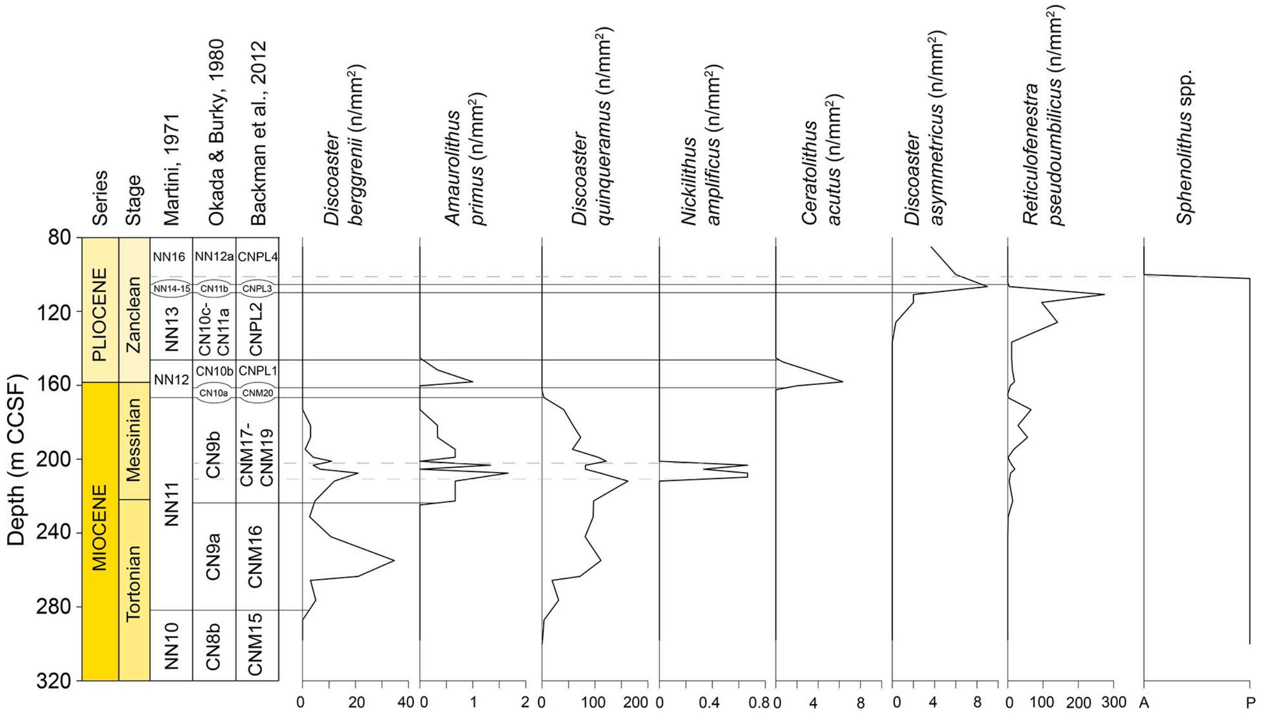

Fig. 2. Number of specimens of selected calcareous nannofossil taxa in a specific area (n/mm^2) across the study interval at IODP Site U1488. For *Spenolithus* spp., "A" means absence and "P" means presence in the sample.

adopted the terms Base absence (Ba) and Top absence (Ta) (Backman et al., 2012) to define intervals in which a taxon temporary shows abundances ranging from very rare to zero and then increases in abundance again, with values comparable to the pre paracme interval. The biostratigraphic schemes applied are those of Martini (1971), Okada and Bukry (1980), and Backman et al. (2012). Taxonomic concepts from several authors and sources are used to determine calcareous nannofossils (Farinacci and Howe, 1969–2022; Perch-Nielsen, 1985; Rio et al., 1990; Raffi and Flores, 1995; and the online atlas Nannotax). We followed Raffi et al. (1998) for classification of *Amaurolithus*, *Nickilithus*, and *Ceratolithus*. *Reticulofenestra pseudoumbilicus* includes placoliths with a long axis exceeding 7 μm as proposed by Raffi and Flores (1995) and Rio et al. (1990). For a qualitative estimation of taxon abundance, we followed the approach proposed by Sutherland et al. (2019).

2.4. *Biostratigraphic age model, sedimentation rates and mass accumulation rates*

Calcareous nannofossil biostratigraphic data have been utilized as tie-points to develop the age model for the study section between 297.86 and 85.02 m. This age model relies on multiple tie-points (Table 1), which integrate both shipboard data and new biostratigraphic data from this study. Calcareous nannofossil biochronologic data are from GTS2020 (Raffi et al., 2020). The positions and the associated ages of each tie-point were used to calculate the linear sedimentation rates (LSR, cm/kyr), assuming the rate remained constant between two successive tie-points.

We calculated the carbonate mass accumulation rates (MAR_{Carb}) at Site U1488 according to:

$$MAR_{Carb} = \%wt\ CaCO_3 * LSR * DBD$$

MAR_{Carb} is expressed as (g cm^{-2} kyr^{-1}). Linear sedimentation rates (LSR; cm/kyr), the carbonate content (%wt $CaCO_3$) and the dry bulk density (DBD; g/cm^3) were derived by linear interpolation from the MAD (Moisture and Density) samples (Suppl. Material S2).

2.5. *Benthic foraminifera*

Quantitative studies on benthic foraminiferal assemblages were carried out on 39 samples between 297.86 and 85.02 m (Suppl. Material S3). The average sampling resolution is 5.5 m, which correspond to ca. 140 kyr resolution. We following the same methodology and taxonomic concepts as outlined in Gastaldello et al. (2023, 2024a). Bulk sediment samples were dried at 40 °C in an oven and weighted to determine the bulk dry sample weight. Then, they were disaggregated in water, washed through a > 63 μm mesh sieve and dried again in an oven at 40 °C. For each sample, ca. 150 to 300 specimens of benthic foraminifera were picked from the >63 μm size fraction and mounted on microslides for permanent record. The scarcity of benthic foraminifera in some samples made it challenging to consistently meet the 300-specimen quota. The >63 μm size fraction is considered to be the one that provides a higher degree of representativeness of the assemblages, since various species are characterised by small adult tests, which would be lost using larger sieve sizes (125 μm, 150 μm, 250 μm). This size fraction allows for more reliable statistical analyses by reducing the number of missing taxa. For species identification, we followed Gastaldello et al. (2024a), Hayward and Buzas (1979), Hayward et al. (2010), Hayward et al. (2013), Hermelin (1989), Holbourn et al. (2013), Kaminski and Gradstein (2005), and Van Morkhoven et al. (1986). Photographs of the most representative specimens were captured using the Scanning Electron Micrograph imaging facilities at the University of Padova (Fig. 3).

We calculated the relative abundance of each species (Fig. 4), the percentage of agglutinated and calcareous hyaline taxa, the Fisher-α diversity (Fisher et al., 1943), and the Shannon-Weaver H(S) heterogeneity index (Murray, 1991) (Fig. 5). Taxa were categorised into infaunal or epifaunal morphogroups based on their morphological characteristics following Corliss (1985, 1991), Jones and Charnock (1985), and Corliss and Chen (1988). The infaunal-epifaunal ratio served as an indicator for assessing trophic conditions and oxygen levels in deep-sea environments. A high prevalence of infaunal species in deep-sea ecosystems is typically associated with eutrophic and/or oxygen-depleted environments, whereas the dominance of epifaunal taxa is indicative of

Table 1

Biohorizons used to biostratigraphically classify the studied section. From left to right: type of event (T, top; Ta, Top Absence; B, base; Ba, Base Absence; Bc, Base Common), species and the base of the biozone they define (Martini, 1971; Okada and Bukry, 1980; Backman et al., 2012), samples and their depths, and the age associated to each biohorizon (GTS2020; Raffi et al., 2020).

Event	Species	Biozone Okada and Bukry (1980)	Biozone Martini (1971)	Biozone Backman et al. (2012)	Depth m CSF top (Rosenthal et al., 2018)	Depth m CSF base (Rosenthal et al., 2018)	Depth m CSF midpoint (Rosenthal et al., 2018)	Depth revised m CCSF top (Drury et al., 2021)[**]	Depth revised m CCSF base (Drury et al., 2021)[**]	Depth revised m CCSF midpoint (Drury et al., 2021)[**]	Depth Error (m revised CCSF; Drury et al., 2021)[**]	Sample top	Sample base	Age (Ma) GTS2020
T	*Discoaster tamalis*[*]	CN12b		CNPL5	68.00	71.00	69.50	74.58	77.58	76.08	1.50	U1488A-8H-4 W, 60–62 cm	U1488A-8H-6 W, 60–62 cm	2.76
T	*Sphenolithus* spp.				90.49	92.50	91.50	100.02	102.16	101.09	1.07	U1488C-10H-5 W, 119–121 cm	U1488B-11H-5 W, 10–12 cm	3.61
T	*Reticulofenestra pseudoumbilicus*	CN12a	NN16	CNPL4	94.72	96.42	95.57	104.38	106.53	105.46	1.08	U1488B-11H-6 W, 82–84 cm	U1488C-11H-3 W, 62–64 cm	3.82
Bc	*Discoaster asymmetricus*	CN11b	NN15+ NN14	CNPL3	96.42	100.82	98.62	106.53	110.81	108.67	2.15	U1488C-11H-3 W, 62–64 cm	U1488B-12H-4 W, 42–44 cm	4.04
T	*Amaurolithus primus*				134.83	139.13	136.98	147.36	151.66	149.51	2.15	U1488C-15H-3 W, 103–105 cm	U1488C-15H-6 W, 82.5–84.5 cm	4.50
T	*Ceratolithus acutus*	CN10c	NN13	CNPL2	132.68	134.83	133.76	145.21	147.36	146.29	1.08	U1488C-15H-2 W, 38–40 cm	U1488C-15H-3 W, 103–105 cm	5.04
B	*Ceratolithus acutus*	CN10b		CNPL1	147.18	149.33	148.26	160.25	162.40	162.33	1.08	U1488C-16H-5 W, 88–90 cm	U1488C-16H-7 W, 3–5 cm	5.36
T	*Discoaster quinqueramus*	CN10a	NN12	CNM20	149.33	148.26	150.27	162.40	164.55	163.48	1.08	U1488C-16H-7 W, 3–5 cm	U1488B-17H-6 W, 30–32 cm	5.53
T	*Nickilithus amplificus*			CNM19	184.79	186.94	185.87	201.11	203.26	202.19	1.07	U1488B-21H-3 W, 39–41 cm	U1488B-21H-4 W, 104–106 cm	5.98
B	*Nickilithus amplificus*			CNM18	192.95	195.10	194.03	209.71	211.86	210.79	1.08	U1488B-22H-2 W, 55–57 cm	U1488B-22H-3 W, 120–122 cm	6.82
Ta	*Reticulofenestra pseudoumbilicus*				212.69	222.76	217.73	231.21	241.96	236.59	5.38	U1488B-24H-2 W, 129-131 cm	U1488B-25H-3 W, 36–38 cm	7.10
B	*Amaurolithus primus*	CN9b			205.06	207.21	206.14	222.61	224.76	223.69	1.07	U1488B-23H-4 W, 16–18 cm	U1488B-23H-5 W, 81–83 cm	7.45
B	*Discoaster quinqueramus*				276.20	277.53	276.87	297.86	300.01	298.94	1.07	U1488A-30H-3 W, 130–132 cm	U1488B-31H-1 W, 113–115 cm	8.10
B	*Discoaster berggrenii*	CN9a	NN11	CNM16	255.95	266.14	261.05	276.36	287.11	281.74	5.38	U1488A-28H-3 W, 5–7 cm	U1488A-29H-3 W, 76–78 cm	8.29
Ba	*Reticulofenestra pseudoumbilicus*[*]			CNM15	286.90	289.90	288.40	310.61	313.61	312.11	1.50	U1488A-31H-4 W, 100–102 cm	U1488A-31H-6 W, 100–102 cm	8.79

[*] Shipboard sample.

[**] Depth revised m CCSF (Drury et al., 2021) is referred to as depth in m.

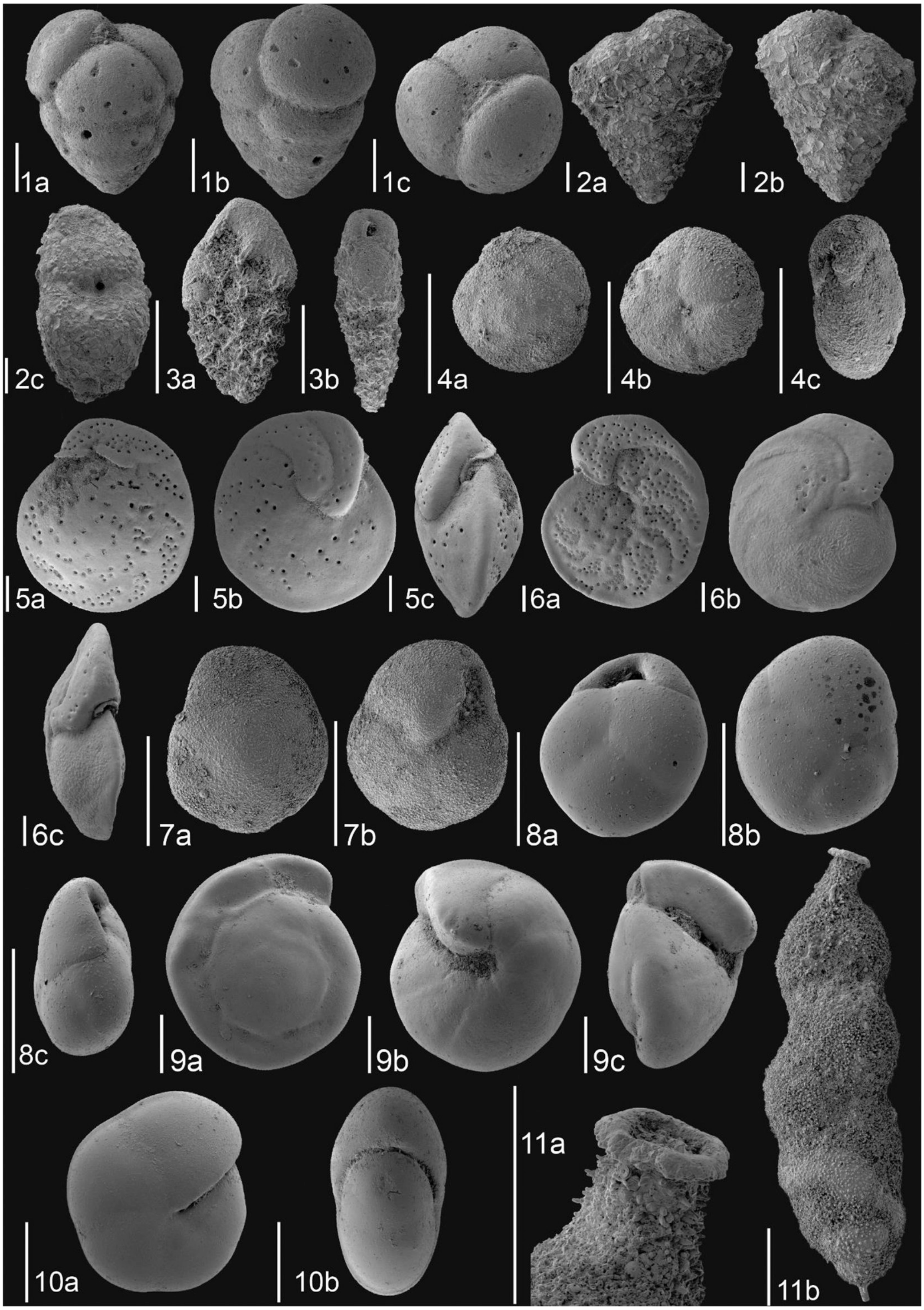

Fig. 3. SEM images of benthic foraminiferal species from Site U1488. **(1)**, *Eggerella bradyi* (sample 20H1, 77–79 cm): a) frontal view; b) side view; c) outline view; **(2)** *Textularia* sp. (sample 20H1, 77–79 cm): a) frontal view; b) lateral side; c) outline view; **(3)** *Abditrodentrix pseudothalmannii* (sample 29H6, 56–58 cm): a) frontal view; b) side view; **(4)** *Alabaminella weddellensis* (sample 20H1, 77–79 cm): a) dorsal side; b) ventral side; c) side view; **(5)** *Cibicidoides mundulus* (sample 12H3, 122–124 cm): a) dorsal side; b) ventral side; c) side view; **(6)** *Cibicidoides wuellestorfi* (sample 10H4, 59–61 cm): a) dorsal side; b) ventral side; c) side view; **(7)** *Epistominella exigua* (sample 13H1, 92–94 cm): a) dorsal side; b) ventral side; **(8)** *Globocassidulina crassa* (sample 18H2, 48–50 cm): a) apertural view; (b) dorsal side; (c) side view; **(9)** *Gyroidina orbicularis* (sample 9H2, 138–140 cm): a) dorsal side; b) ventral side; c) side view; **(10)** *Pullenia quinqueloba* (samples 9H2, 138–140 cm): (a) side view, (b) apertural view; **(11)** *Uvigerina proboscidea* (sample 29H6, 56–58 cm): a) aperture; b) frontal view. All scale bars = 100 μm.

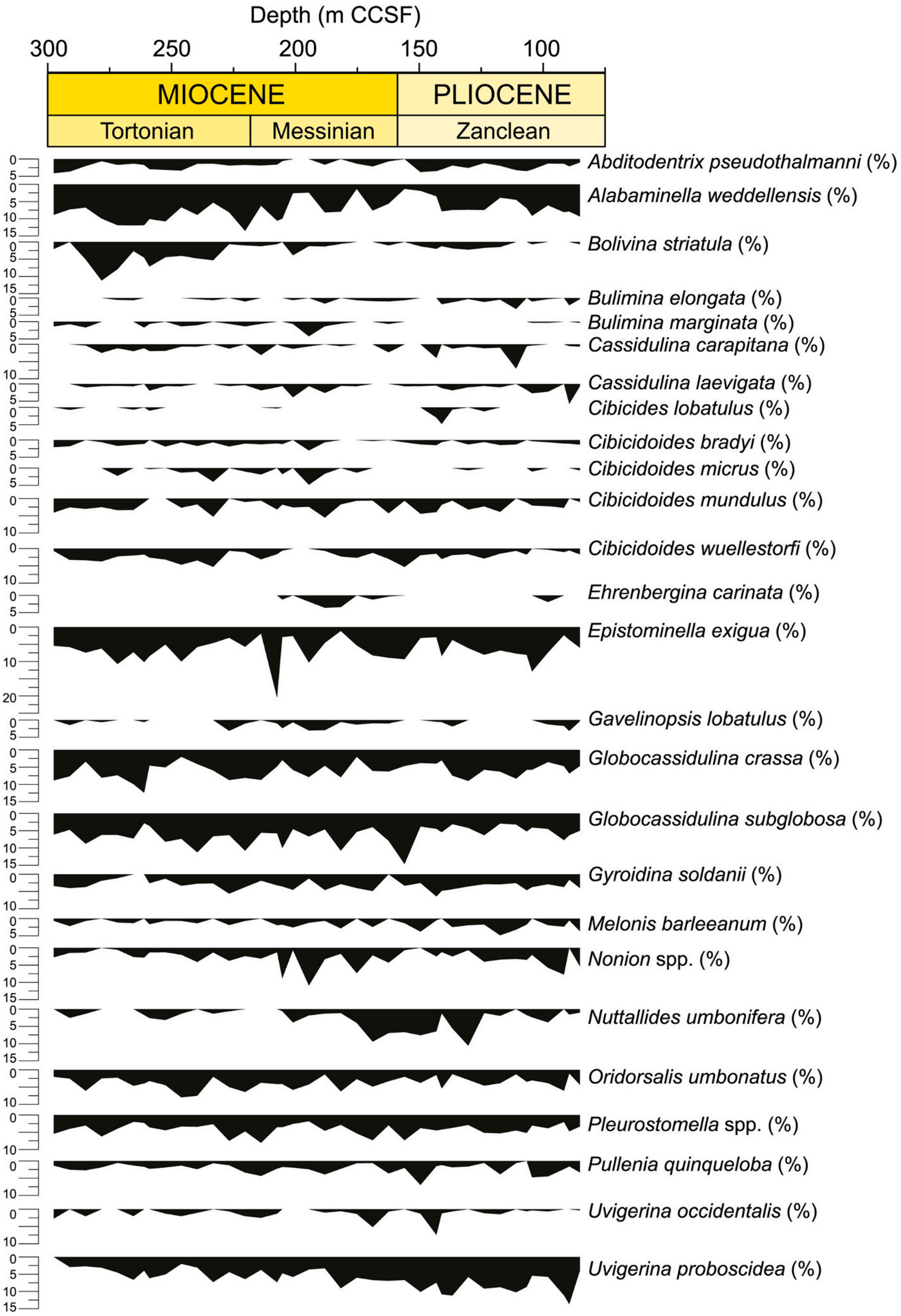

Fig. 4. Relative abundance of significant benthic foraminiferal species (>3 % of the assemblages in at least one sample) at IODP Site U1488.

oligotrophic conditions and/or high oxygen availability (Jorissen et al., 1995, 2007). We further categorised the relative abundance of species sharing similar paleoecological characteristics, calculating the percentage of phytodetritus exploiting taxa (PET; Gooday, 1988, 1993; Suhr et al., 2003; Jorissen et al., 2007; Boscolo-Galazzo et al., 2015) and suboxic-dysoxic taxa (Bernhard, 1986; Kaiho, 1991).

Statistical analyses were carried out on a dataset of species with a relative abundance >3 % in at least one sample (Fig. 4). We conducted a hierarchical cluster analysis using the PAST software (Hammer et al., 2001) using the unweighted pair-group average algorithm (UPGMA) and the Pearson correlation (Suppl. Material S4), and a Detrended Correspondence Analysis (DCA) in R-mode (species; Fig. 6) and Q-mode (samples; Fig. 7) to investigate the relationship between benthic foraminiferal assemblages and environmental variables (Hammer and Harper, 2005).

We categorised each species into three groups: Dysoxic “D”, Suboxic “S”, and Oxic “O” based on criteria established by Bernhard (1986), Kaiho (1991), and on existing benthic foraminifera oxygen preferences documented in the literature (Kaiho, 1994, 1999; Loubere, 1994; Fariduddin and Loubere, 1997; Schmiedl et al., 1997; Bernhard and Sen Gupta, 1999; de Rijk et al., 2000; Fontanier et al., 2002; Jorissen et al., 2007; Kranner et al., 2022;). We calculated the Enhanced Benthic Foraminifera Oxygen Index (EBFOI, Fig. 5; Suppl. Material S4), as described by “Eq. (3)” in Kranner et al. (2022):

$$EBFOI = 100^{*}\left(\frac{O}{O + D + \frac{S}{2}}\right)$$

We opted for these EBFOI index over the original Benthic

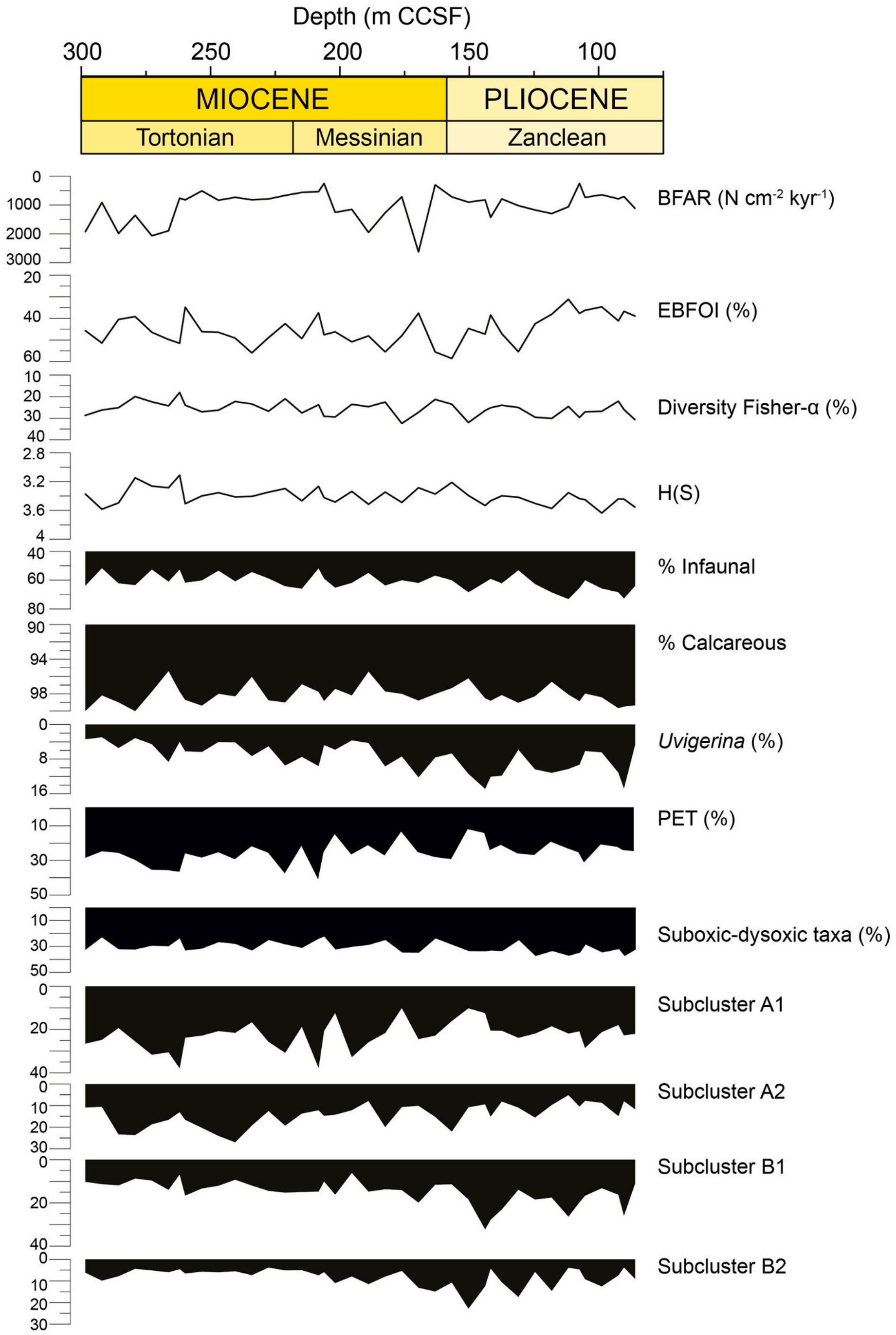

Fig. 5. Benthic foraminifera quantitative analysis: BFAR, EBFOI, Fisher-α diversity index, Shannon-Weaver H(S) heterogeneity index, percentage of infaunal morphogroup, percentage of calcareous taxa, relative abundance of *Uvigerina* species, phytodetritus exploiting taxa (PET), dysoxic-suboxic taxa, and relative abundance of Subclusters A1, A2, B1, and B2 plotted against depth (m CCSF).

Foraminifera Oxygenation Index (BFOI; Kaiho, 1991) because the former includes the dysoxic species, which were omitted from the original equation.

We use benthic foraminiferal accumulation rates (BFAR, expressed as Number of foraminifera N cm^{-2} kyr^{-1}, Fig. 5; Suppl. Material S5) as a semi-quantitative proxy for estimation of export productivity (Jorissen et al., 2007). BFAR was calculated following the equation proposed by Herguera and Berger (1991).

$$BFAR = (nr/g > 63\,\mu m * \%wt > 63/100) * LSR * DBD$$

Where, nr/g > 63 μm is the number of benthic foraminifera per gram of sediment from the >63 μm fraction; %wt >63 μm is the weight percentage of foraminifera in >63 μm fraction of the sample; LSR is the linear sedimentation rate (cm/kyr); and DBD is the dry bulk density (g cm^{-3}) interpolated from the shipboard data (Rosenthal et al., 2018).

3. Results

3.1. Calcareous nannofossil biostratigraphy and preservation

Calcareous nannofossils are generally abundant and exhibit moderate to good preservation throughout the studied succession. The genus *Discoaster* is common to abundant (0–100 specimens per field of view) throughout the study interval, while the abundance of *Reticulofenestra*

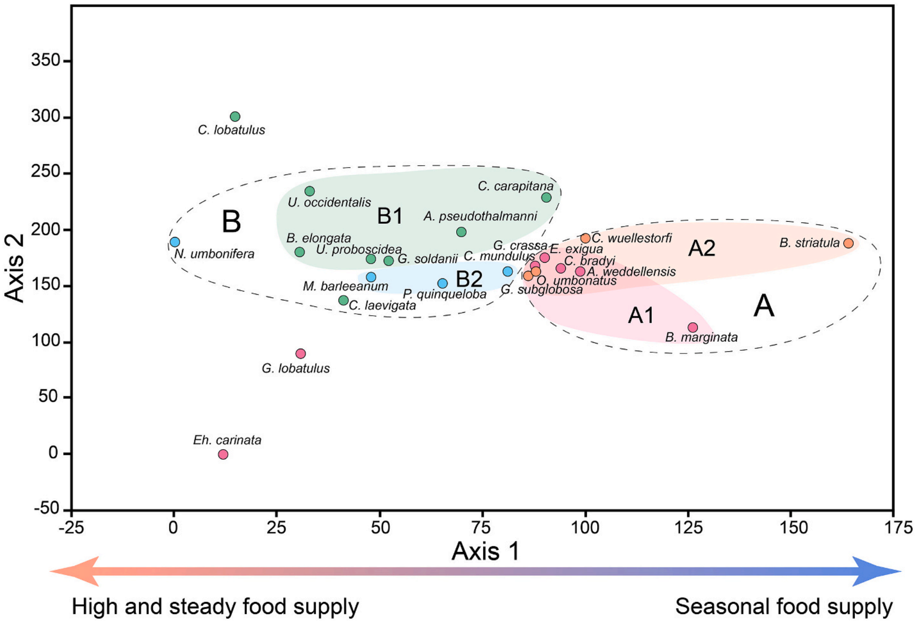

Fig. 6. R-mode (species) Detrended Correspondence Analysis (DCA) of benthic foraminiferal assemblages from Site U1488. Subcluster A1 (pink), A2 (orange), B1 (green), and B2 (blue). The main axis controlling sample distribution is Axis 1, low values along this axis indicate continuous input of nutrients, while high values are linked to pulsed supply of nutrients to the seafloor. (For interpretation of the references to colour in this figure legend, the reader is referred to the web version of this article.)

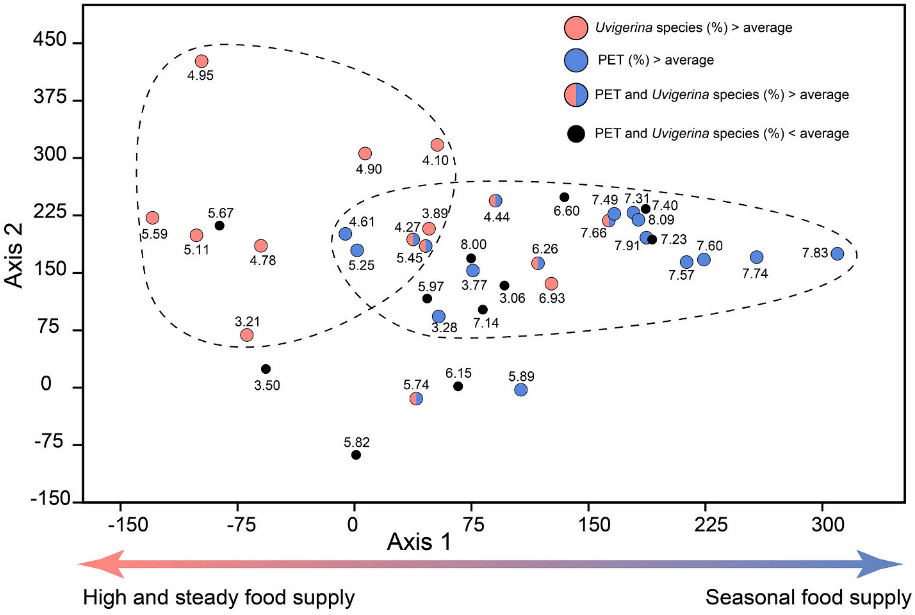

Fig. 7. Q-mode (samples) Detrended Correspondence Analysis (DCA) of benthic foraminiferal assemblages from Site U1488. Sample ages have been used instead of the sample's IDs. We distinguished four groups based on the relative abundance of *Uvigerina* species and PET in each sample. The main axis controlling sample distribution is Axis 1, low values along this axis indicate continuous input of nutrients, while high values are linked to pulsed supply of nutrients to the seafloor.

pseudoumbilicus goes from few (1 specimen per 1–10 fields of view) to common (>1–10 specimens per field of view). *Amaurolithus*, *Ceratolithus* and *Nickilithus* are rare to very rare (<1 specimen per 10 fields of view). Semiquantitative counts (specimens/mm^2) of *Calcidiscus macintyrei* and *Sphenolithus abies* were not carried out, and presence-absence data is provided only.

Preservation of the single specimens varied significantly based on the taxon. *Discoaster* are generally well preserved. *Amaurolithus*, *Ceratolithus*, and *Nickilithus* show a moderate preservation, and although the principal morphological characteristics are slightly altered and show overgrowth (particularly *Ceratolithus*), the diagnostic features for species identification are still recognizable. The selected biohorizons are presented in Table 1, arranged in chronological order from younger to older. For each biohorizon, we provide the use within the adopted biostratigraphic schemes, the position at Site U1488, the abundance pattern associated with the event, and an evaluation of its reliability in comparison to existing literature data.

3.1.1. Top *Sphenolithus*

The disappearance (Top) of the genus *Sphenolithus* is not used for defining a zonal boundary, however, it serves as a valuable secondary biostratigraphic datum (Backman et al., 2012). With an estimated age of 3.61 Ma (Raffi et al., 2020), this event is generally observed after the disappearance (Top) of *R. pseudoumbilicus*, within Zone CNPL4 (Backman et al., 2012). At Site U1488, this biohorizon has been identified between samples U1488B-11H-5 W, 10–12 cm and U1488C-10H-5 W, 119–121 cm, at 101.09 (± 1.07) m.

3.1.2. *Top Reticulofenestra pseudoumbilicus*

At Site U1488, we recorded the disappearance (Top) of *R. pseudoumbilicus* between samples U1488C-11H-3 W, 62–64 cm and U1488B-11H-6 W, 82–84 cm, at 105.46 (± 1.08) m, where the abundance of *R. pseudoumbilicus* decreases from 100 to 130 to 0 specimens per mm^2. This event marks the base of Zone NN16 (Martini, 1971), of Subzone CN12a (Okada and Bukry, 1980), and of Zone CNPL4 (Backman et al., 2012).

Consistently with the literature, the disappearance of *R. pseudoumbilicus* at Site U1488 lies between the Base common of *Discoaster asymmetricus* and the Top of the genus *Sphenolithus*. This biohorizon has an estimated age of 3.82 Ma and was evaluated by Raffi et al. (2020) with the maximum degree of reliability. Moreover, several studies have reported this event to be synchronous (e.g., Backman and Shackleton, 1983; Young, 1990; Shackleton et al., 1995; Gastaldello et al., 2023).

3.1.3. *Base common Discoaster asymmetricus*

The Base Common of *D. asymmetricus* marks the base of merged Zone NN14/NN15 (Martini, 1971), the base of Subzone CN11b (Okada and Bukry, 1980), and the base of Zone CNPL3 (Backman et al., 2012). At Site U1488, this event occurs between samples U1488B-12H-4 W, 42–44 cm and U1488C-11H-3 W, 62–64 cm, at 108.68 (± 2.15) m, with an estimated age of 4.04 Ma (Raffi et al., 2020).

This biohorizon is considered reliable and fairly isochronous (Raffi et al., 2020). When comparing data from this study with data generated from ODP Site 1085 (southeast Atlantic Ocean; Gastaldello et al., 2024b), it is evident that *D. asymmetricus* exhibits a significantly lower abundance at Site U1488. Nevertheless, the abundance pattern observed at Site U1488 aligns consistently with the abundance pattern observed at ODP Site 1085.

3.1.4. *Top Amaurolithus primus*

The disappearance (Top) of *A. primus* occurs between samples U1488C-15H-6 W, 83–85 cm and U1488C-15H-3 W, 103–105 cm, at 149.51 (± 2.15) m, with an estimated age of 4.50 Ma (Raffi et al., 2020). This event is excluded from the biozonations used in this study, however, it is a notable secondary biostratigraphic datum observed within Zone CNPL2 (Backman et al., 2012).

According to Raffi and Flores (1995), the extinction pattern of various ceratolithids species (including *A. primus*) has been poorly recorded at different locations (e.g., Berggren et al., 1985), resulting in a diachronous age estimation for the disappearance of these species. Moreover, several studies documented a general low and uneven occurrence of *A. primus*, especially in the final tail of its distribution, thereby suggesting to avoid the use of the Top of *A. primus* (Backman et al., 2012; Raffi et al., 2020; Gastaldello et al., 2023). At Site U1488, the abundance of *A. primus* is rare/scarce and displays a scattered pattern that makes it difficult to the locate of the top event. Since the disappearance of *A. primus* does not seem to represent a reliable marker, we prefer not to use this biohorizon as a tie-point in our age model.

3.1.5. *Base and Top of Ceratolithus acutus*

At Site U1488, *Ceratolithus acutus* appears between samples U1488C-16H-7 W, 3–5 cm and U1488C-16H-5 W, 88–90 cm, at 161.33 (± 1.08) m and disappears between samples U1488C-15H-3 W, 103–105 cm and U1488C-15H-2 W, 38–40 cm, at 146.29 (± 1.08) m. The total range of *C. acutus* marks Subzone CN10b (Okada and Bukry, 1980) and Zone CNPL1 (Backman et al., 2012).

Ceratolithus acutus shows a continuous abundance pattern on a short stratigraphic range at Site U1488, consistent with the literature (Backman and Raffi, 1997; Raffi et al., 1998; Backman et al., 2012). Both the Base and the Top of *C. acutus* are considered isochronous and reliable events, with estimated ages of 5.36 Ma and 5.04 Ma, respectively (Raffi et al., 2020).

3.1.6. *Top Discoaster quinqueramus*

The disappearance (Top) of *D. quinqueramus* defines the base of Zone NN12 (Martini, 1971), Subzone CNM10a (Okada and Bukry, 1980) and Zone CNM20 (Backman et al., 2012). The continuous presence and then neat decrease in abundance of *D. quinqueramus* allowed to precisely position the final exit of this taxon between samples U1488B-17H-6 W, 30–32 cm and U1488C-16H-7 W, 3–5 cm at 163.48 (± 1.08) m, with an estimated age of 5.53 Ma (Raffi et al., 2020).

This event is considered a well-defined and reliable biohorizon, globally isochronous (Backman et al., 2012; Raffi et al., 2020). The observed abundance pattern at Site U1488 compares well with previous data available from the Atlantic Ocean (Marino and Flores, 2002) and the Pacific Ocean (Gastaldello et al., 2023), confirming the high reliability of this event.

3.1.7. *Base and Top of Nickilithus amplificus*

Nickilithus amplificus appears between samples U1488B-22H-3 W, 120–122 cm and U1488B-22H-2 W, 55–57 cm, at 210.79 (± 1.08) m and disappears between samples U1488B-21H-4 W, 104–106 cm and U1488B-21H-3 W, 39–41 cm, at 202.19 (± 1.07) m. The total range of *N. amplificus* defines Zone CNM18 (Backman et al., 2012). This taxon range zone corresponds to the upper part of Zone NN11 (Martini, 1971) and the middle part of Subzone CN9b (Okada and Bukry, 1980).

At Site U1488, *Nickilithus amplificus* shows a continuous abundance pattern and the typical short stratigraphic range consistent with the literature (Raffi et al., 1998). The abundance pattern observed at Site U1488 is consistent with previous data from the Atlantic Ocean (Gastaldello et al., 2024b) and the Pacific Ocean (Gastaldello et al., 2023). The Base and Top of *N. amplificus*, documented after the appearance of the genus *Amaurolithus* (i.e., *Amaurolithus primus* and *Amaurolithus delicatus*), and before the first appearance of the genus *Ceratolithus* (i.e., *Ceratolithus acutus* and *Ceratolithus cristatus*), respectively, are consistent with the *Amaurolithus* – *Nicklithus* – *Ceratolithus* evolutionary lineage (Raffi et al., 1998). However, due to the overall low abundance of these taxa throughout the study section, the precise positioning of each individual event may potentially be asynchronous. To address this issue, it would be necessary to study these events at a very high resolution in successions with an independent age model based on magnetostratigraphy, or astronomically tuned.

3.1.8. *Top absence Reticulofenestra pseudoumbilicus*

The Top Absence of *R. pseudoumbilicus* defines the end of the paracme interval of this taxon. This biohorizon is not used to define a zonal boundary, but occurs within Zone CNM17 (Backman et al., 2012), with an estimated age of 7.10 Ma (Raffi et al., 2020). At Site U1488, no specimens of *R. pseudoumbilicus* have been encountered between 297.86 and 223.69 (± 2.15) m. The end of the paracme event is located between sample U1488B-23H-5 W, 81–83 cm and sample U1488B-23H-4 W, 16–18 cm, where the abundance of *R. pseudoumbilicus* starts to increase and reaches values around 50–100 specimens per mm^2.

For biostratigraphic analyses, *R. pseudoumbilicus* exclusively comprises placoliths with a long axis > 7 μm, following Rio et al. (1990) and Raffi and Flores (1995). Nonetheless, emerging evidence suggests that factors such as nutrient availability, temperature, light intensity, Mg/Ca ratio may have influenced alterations in coccolith morphology (Faucher et al., 2020). This suggests a probable diachronism arising from variations in environmental conditions across different locations. Furthermore, this event has been classified as indistinct and poorly defined in terms of abundance pattern (Raffi et al., 2020; Gastaldello et al., 2023).

3.1.9. Base of *Amaurolithus primus*

The first occurrence (Base) of *A. primus* defines the base of Subzone CN9b (Okada and Bukry, 1980) and the base of Zone CNM17 (Backman et al., 2012). At Site U1488, this event is positioned between sample U1488B-23H-5 W, 81–83 cm and sample U1488B-23H-4 W, 16–18 cm at 223.69 (± 1.07) m. In the literature, the Base of *A. primus,* which coincides with the base of the genus, is considered to be a reliable biohorizon with an estimated age of 7.45 Ma (Raffi et al., 2020). However, due to the low and scattered abundance of this taxon at Site U1488, the positioning of this event is extremely difficult. For this reason, we decided not to incorporate this biohorizon in our age model.

3.1.10. Base of *Discoaster quinqueramus*

The Base of *D. quinqueramus* marks the base of Zone NN11 (Martini, 1971). At Site U1488, this event occurs between sample U1488B-31H-1 W, 113–115 cm and sample U1488A-30H-3 W, 130–132 cm at 298.94 (± 1.07) m. *Discoaster quinqueramus*, as the other *Discoaster* documented at Site U1488, shows an increasing trend in the abundance pattern from 1 to 3 specimens per mm^2 around 292.49 m, to a maximum of 162 specimens per mm^2 at 211.86 m. This event has an estimated age of 8.10 Ma and has been defined as “poorly reliable” by Raffi et al. (2020).

3.1.11. Base of *Discoaster berggrenii*

The appearance (Base) of *D. berggrenii* occurs between sample U1488A-29H-3 W, 76–78 cm and sample U1488A-28H-3 W, 5–7 cm at 281.74 (± 5.38) m. It marks the base of Subzone CNM9a (Okada and Bukry, 1980) and the base of Zone CNM16 (Backman et al., 2012).

According to Raffi et al. (1998), both *D. quinqueramus* and *D. berggrenii* evolved from *Discoaster bellus*. Due to the gradual evolution of this lineage and to the presence of intermediate forms, the identification of the Base of *D. berggrenii* is typically difficult and can influence the degree of synchrony/diachrony of this event in different areas (for details, see Backman and Raffi, 1997). *Discoaster berggrenii* shows a high abundance pattern, with an average abundance of 10 specimens per mm^2 and a peak of 34 specimens per mm^2 at 254.86 m.

3.2. Benthic foraminiferal assemblages

Benthic foraminiferal tests are generally well preserved across the studied interval. We recognised a total of 90 taxa (80 calcareous taxa and 10 agglutinated taxa) at the species or higher taxonomic levels (Suppl. Material S3). Calcareous hyaline taxa dominate the benthic foraminiferal assemblages (up to 99 % of the assemblages), and agglutinated species only make up at most 5 % of the assemblages (Fig. 5). The distribution of infaunal and epifaunal morphogroups remains consistent throughout the study interval, and infaunal taxa are more abundant (60–70 % of the assemblages) than epifaunal ones. Among infaunal species, *Bolivina striatula*, *Globocassidulina crassa* (Fig. 3(8)), *Globocassidulina subglobosa*, and *Uvigerina proboscidea* (Fig. 3(11)) are the most abundant. Among epifaunal taxa, *Alabaminella weddellensis* (Fig. 3(4)), *Cibicidoides mundulus* (Fig. 3(5)), *Epistominella exigua* (Fig. 3(7)), and *Nuttallides umbonifera* dominate. The Fisher-α diversity index (Fig. 5) ranges between 18.07 (at 261.31 m) and 32.41 (at 175.3 m). The lowest values are reached in the lowermost part of the studied interval, between 281.74 and 260.24 m, and gradually increase towards the top. The Shannon-Weaver heterogeneity index H(S) ranges between 3.11 and 3.64, with a minimum value in the lower part of the studied interval, at 261.31 m, and its maximum value at 97.92 m (Fig. 5). The relative abundance of most of the species observed in this study is generally low (< 2 % in more than half of the samples) and not continuous.

The abundance of the phytodetritus exploiting taxa (PET) group ranges between 12 and 42 % of the assemblages, mainly represented by *A. weddellensis, E. exigua*, and *G. crassa,* (Fig. 4). The highest abundance is recorded in the lower part of the studied interval, between 297.86 and 206.47 m. Opportunistic taxa exhibit a trend similar to that of the PET group (Fig. 5), with the relative abundance ranging from 17 to 44 % and the highest values occurring in the lower part of the studied section (297.86 to 206.47 m). Suboxic-dysoxic taxa, such as *B. striatula*, *Bulimina truncana* and *U. proboscidea*, make up between 22 % and 37 % of the assemblages, with minimum values in the middle part of the study interval (Fig. 5).

The EBFOI values (Fig. 5) range from a minimum of 31.16 (at 110.82 m) to a maximum of 58.56 (at 155.95 m). The EBFOI shows several fluctuations in the lower and middle part of the studied interval, ranging from ca. 35–40 to ca. 50–60. From 110.82 m to the top, we documented the lowest values (ca. 30–40). The BFARs show low values in the lowermost part of the study interval, between 297.86 and 205.41 m. After a first increase between 205.41 and 162.40 m, where the maximum values are recorded (2629 at 168.85 m), a second increase is documented between 162.40 and 106.53 m (maximum value 1430 at 140.92 m). In the uppermost part of the studied section, BFARs show values around 700–1000, with an upward increasing trend (Fig. 5).

The hierarchical cluster analysis of species ($n = 23$) shows two main clusters (A and B) and four subclusters: A1, A2, B1, B2. Subcluster A1 contains seven species, and the most common species are the main representatives of the PET group. The relative abundance of this subcluster ranges from 10 % to 37.9 % across the studied interval. This subcluster shows an upward decreasing trend, with the highest values documented between 297.86 and 246.26 m, highly oscillating values between 246.26 and 149.51 m, with a return to steady values of around 20 % in the uppermost part of the studied interval. Subcluster A2 includes four species, *B. striatula*, *Cibicidoides wuellestorfi* (Fig. 3(6)), *G. subglobosa*, and *Oridorsalis umbonatus*. The relative abundance of this subcluster ranges between 5.1 and 26.9 %, showing an upward decreasing trend with high values (around 20–25 %) between 297.86 and 207.53 m, and lower values (around 10 %) in the rest of the study interval.

Subcluster B1 is the most diverse one, including eight species. *Uvigerina proboscidea* is the most abundant species, followed by *Gyroidina soldanii*. The relative abundance of this subcluster spans from 6.1 to 32.2 %, with values around 10 % in the lower part up to 155.95 m, and an increase (up to 20–30 %) in the upper part, between 155.95 and 85.02 m. Subcluster B2 contains 4 species, *C. mundulus*, *Melonis barleeanum*, *N. umbonifera*, and *Pullenia quinqueloba* (Fig. 3(10)). The relative abundance of this subcluster ranges from 3.7 to 22.8 % across the study interval, recording low values (around 5–10 %) between 297.86 and 175.30 m. In the upper part, between 175.30 and 85.02 m, the relative abundance reaches values around 20 %, with the highest value documented at 149.51 m.

On the same dataset as the cluster analysis (species >3 % in relative abundance), we performed a DCA analysis in R-mode (species) and a Q-mode (samples) to further study the environmental variables that influenced the distribution pattern of benthic. In the R-mode (species), species were grouped into the four subclusters differentiated in the hierarchical cluster analysis (Fig. 6). Species are more spread along Axis 1, with subclusters B1 and B2 dominating at low values, and subclusters A1 and A2 located at high values. Only one outlier (*Cibicides lobatulus*) was found to be outside the 95 % confidence ellipse. In the Q-mode (samples), samples are spread along Axis 1, with samples from the lower part of the studied interval (between 297.86 and 205.41 m) located at high values, and samples from the upper part (205.41 and 85.02 m) located at lower values along the axis (Fig. 7).

Two-thirds of the samples analysed have fewer than 300 benthic foraminifera, which could introduce limitations in the dataset. This low count may impact the accuracy of diversity estimates and the overall robustness of our numerical analyses, potentially affecting the reliability of the paleoenvironmental interpretations. A key issue associated with low counts is the increased likelihood of missing rare species, which can result in an underestimation of species diversity. However, our dataset shows no apparent correlation between low counts and species diversity, and some low-count samples exhibit higher diversity than those with higher counts (Suppl. Material S6). Moreover, this issue does not seem to influence any particular cluster in the statistical analyses, and for instance, examination of the Q-mode (samples) DCA reveals that each group includes samples with both high and low benthic foraminiferal counts.

4. Improved biostratigraphic age model and identification of the Biogenic Bloom in the WEP

4.1. Improved biostratigraphic age model

Based on the age model, the investigated section at Site U1488 spans from 8.8 Ma (Late Miocene) to 2.8 Ma (Late Pliocene) (Fig. 8; Suppl. Material S7). Calcareous nannofossil biostratigraphic data have been used as tie-points to develop the age model between 297.86 and 85.02 m of the study section (ca. 8.1–3.1 Ma). As previously discussed, not all of the biohorizons identified and described in paragraph 3.1 were taken into consideration. For instance, as noted in the IODP U1488 Report (Rosenthal et al., 2018), establishing biohorizons by relying on the presence of species within the *Amaurolithus* lineage presents difficulties due to the infrequent and irregular occurrence of these species. Even though we prepared very dense smear slides, *Amaurolithus primus* still displays a very rare and scattered abundance, making the positioning of this event difficult. The Base of *N. amplificus* is another possible unreliable event, and it was not considered in the age model. It has been documented, as expected, after the appearance of genus *Amaurolithus*; the short stratigraphic range and the low abundance of *N. amplificus* possibly affect the finding of the first forms, and a higher resolution sampling would be needed to define this event at Site U1488. The typical sequence of documentation shows the Base of *D. berggrenii* preceding the appearance of *D. quinqueramus*. However, at Site U1488, we have observed the first appearance of *D. berggrenii* occurring after the Base of *D. quinqueramus*. This discrepancy in the abundance pattern of *D. berggrenii* may be attributed to significant recrystallization of this taxon, making it challenging to differentiate between *D. berggrenii* and *D. quinqueramus*. Due to this uncertainty, to construct the age model we decided to use the Base of *D. quinqueramus* rather than the Base of *D. berggrenii.*

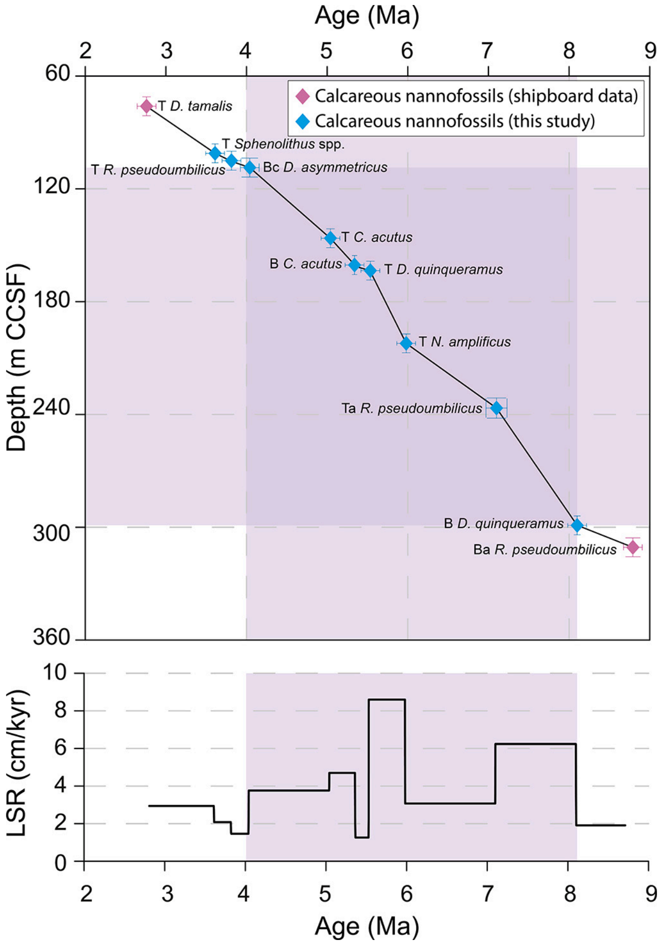

Fig. 8. Age model and linear sedimentation rates at IODP Site U1488. Highlighted in purple: the Biogenic Bloom interval. (For interpretation of the references to colour in this figure legend, the reader is referred to the web version of this article.)

4.2. Sedimentation rates, MARs and identification of the biogenic bloom

Based on the improved age model, we calculated the linear sedimentation rates (LSRs), which show high values (ca. 7.5 cm/kyr) between 8.1 and 7.1 Ma (from 297.52 to 237.97 m), then values drop to ca. 2–3 cm/kyr, between 7.1 and 6.0 Ma (from 237.97 to 201.36 m). A sharp increase is recorded between 6.0 and 5.5 Ma (from 201.36 to 164.44 m), with a peak of 8.6 cm/kyr. A secondary interval of high LSR spans from 5.4 to 4.0 Ma (from 160.59 to 112.25 m) with values around 4–5 cm/kyr. From 4.0 Ma to the top of the study section (from 112.25 to 77.50 m), LSRs decrease and reach values around 2–3 cm/kyr (Fig. 8).

The increase in $\mathrm{MAR_{Carb}}$ is a frequently used proxy for identifying the Biogenic Bloom (e.g., Farrell et al., 1995; Zhang et al., 2009; Lyle et al., 2019; Drury et al., 2021; Gastaldello et al., 2023, 2024b). $\mathrm{MAR_{Carb}}$ consistently follows the LSR trend. The interval between 8.1 and 7.1 Ma shows high $\mathrm{MAR_{Carb}}$ values around 7.5 g $\mathrm{cm^{-2}\ kyr^{-1}}$. Values drop down to 3 g $\mathrm{cm^{-2}\ kyr^{-1}}$ between 7.1 and 6.0 Ma, and then increase up to 9.7 g $\mathrm{cm^{-2}\ kyr^{-1}}$ between 6.0 and 5.5 Ma. A lesser increase is documented between 5.5 and 4.0 Ma, where $\mathrm{MAR_{Carb}}$ reaches values around 3–4 g $\mathrm{cm^{-2}\ kyr^{-1}}$. The lowest $\mathrm{MAR_{Carb}}$ values (around 2–3 g $\mathrm{cm^{-2}\ kyr^{-1}}$) are recorded in the uppermost part of the studied interval, between 4.0 and 3.1 Ma shows.

The overall increase in $\mathrm{MAR_{Carb}}$ between 8.1 and 4.0 Ma at Site U1488 is interpreted as the manifestation of the Biogenic Bloom. At Site U1488, the Biogenic Bloom exhibits a fluctuating pattern, characterised initially by a phase of elevated $\mathrm{MAR_{Carb}}$ values spanning from 8.1 to 7.1 Ma, succeeded by a decline between 7.1 and 6.2 Ma. The increase in $\mathrm{MAR_{Carb}}$ at 8.1 Ma is indicative of the onset of the Biogenic Bloom in the WEP. Although the biostratigraphic age model here is not astronomically tuned, the onset of the Biogenic Bloom in the WEP appears to be consistent with the timing of the onset in the EEP and SE Atlantic (Drury et al., 2018; Drury et al., 2021; Gastaldello et al., 2024b). The termination of the Biogenic Bloom in the WEP appears to occur after the termination in the EEP and other low-latitude regions (ca. 4.6–4.4 Ma; Lyle et al., 2019; Karatsolis et al., 2022), but significantly before the termination in the SE Atlantic (ca. 3.3 Ma; Drury et al., 2021).

5. Interpretation and discussion

5.1. WEP deep sea ecology and paleoenvironmental interpretation

Changes in benthic foraminiferal assemblages across the studied interval provide information about their ecological response across the Biogenic Bloom. Subcluster A1 includes some of the most abundant species: *A. weddellensis*, *E. exigua*, and *G. crassa*. These PET group species are typically associated to oxic conditions and background trophic states with seasonal input of phytodetritus from the surface waters due to extensive phytoplankton blooms (Gooday, 1993; Smart et al., 1994; Jorissen et al., 2007; Corliss et al., 2009). The relative abundance of Subcluster A1 is higher between 8.1 and 6.2 Ma, then it fluctuates but shows an overall decreasing trend up to 4.9 Ma, and it increases between 4.9 and 3.1 Ma (Fig. 9). The persistent high abundance of PET

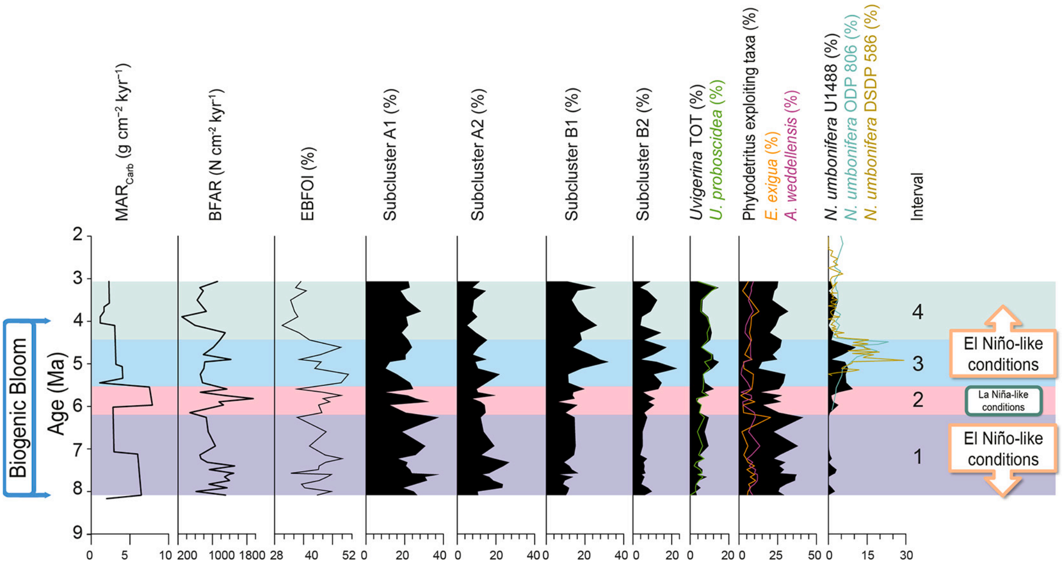

Fig. 9. MAR_{Carb}, BFAR, EBFOI, relative abundance of Subclusters A1, A2, B1, and B2, relative abundance of *Uvigerina* species (*U. proboscidea* in green), of phytodetritus exploiting taxa (*E. exigua* in orange and *A. weddellensis* in pink*)*, and of *N. umbonifera* (Site U1488 in black, Site 806 in light blue, Site 586 in gold), and intervals plotted against age (Ma). On the right, El Niño-like conditions and La Niña-like conditions from Drury et al. (2018) (For interpretation of the references to colour in this figure legend, the reader is referred to the web version of this article.)

throughout the entire study interval suggests sustained phytoplankton blooms act as the main benthic the food supply at Site U1488.

Subcluster A2 shows an upward decreasing trend, with the highest relative abundance between 8.1 and 6.2 Ma (Fig. 9). *Globocassidulina subglobosa* and *O. umbonatus* are the dominant taxa of this subcluster. The former is one of the most abundant species at this site and is part of the PET group, confirming the importance of this group throughout the study interval. Assemblages characterised by the co-dominance of *O. umbonatus* and *G. subglobosa* have been reported to be indicative of high oxygen levels and carbonate corrosiveness at the seafloor (e.g., Murray, 1988; Mackensen et al., 1995; Hayward et al., 2004).

Subcluster B1 shows an overall upward increasing trend (Fig. 9) and is dominated by suboxic-dysoxic indicators such as *B. elongata*, *C. laevigata*, *U. proboscidea*, and *U. occidentalis.* The increase in the B1 subcluster combined with the R-mode DCA analysis (Fig. 6) points to eutrophic conditions at the seafloor (confirmed also by the R-mode DCA analysis, Fig. 6), a sustained input of food and low oxygen levels at the seafloor. Subcluster B2 is dominated by *N. umbonifera*, an epifaunal species typically associated with low temperature, oxic conditions, low food supply and corrosive bottom water (Bremer and Lohmann, 1982; Gooday, 1994; Gupta, 1997; Loubere and Fariduddin, 1999; Smart et al., 2007). The high abundance of corrosion-resistant species (e.g., *N. umbonifera*) and the 10–20 % decline in $CaCO_3$% from 5.9 Ma upward might point to enhanced $CaCO_3$ corrosivity of bottom waters. However, the composition and general preservation of assemblages does not support significant carbonate dissolution at the seafloor, as calcareous taxa significantly dominate the assemblages (Fig. 5).

The combining evidence of observed changes in benthic foraminiferal assemblages suggests Site U1488 was dominated by a pulsed, high nutrient input and high oxygen during the Late Miocene-Early Pliocene at Site U1488. This is further supported by the EBFOI and BFAR. The EBFOI indicates sustained oxic conditions, with a slight decrease towards suboxic conditions around 4.5 Ma, while the BFAR points to high export productivity between 8.1 and 4.0 Ma, which is particularly high from 6.2 to 5.5 Ma (Fig. 9).

The R-mode (species) analysis (Fig. 6) groups species from Cluster A towards more positive values along axis 1. The most abundant species from Subclusters A1 and A2 (e.g., *A. weddellensis, E. exigua, G. crassa*) belong to PET, which are usually related to increased seasonality of the food input to the seafloor. Negative values along this axis include species indicative of high and continuous food supply (e.g., *B. elongata, C. laevigata, U. proboscidea*). We suggest Axis 1 is controlled by the food supply to the seafloor, with a steadier input of food at low values and high seasonal food supply at high values.

In the Q-mode (samples) analysis (Fig. 7), Axis 1 is identified as the primary axis controlling the distribution of samples. We distinguished two groups based on the taxa dominating in each sample. Samples with a PET relative abundance surpassing the mean value are depicted in orange, and samples with a higher-than-average relative abundance of *Uvigerina* species are represented in blue. Axis 1 seems to be controlled by the type and the amount of food reaching the seafloor. We observed that samples from ca. 8.1–6.2 Ma (297.86 to 205.41 m) are mainly located at high values along Axis 1, pointing to seasonal influx of phytodetritus. Samples from ca. 5.3–3.1 Ma (159.18 to 85.02 m) are found at low values along Axis 1, where the high abundance of *Uvigerina* species points to more eutrophic conditions due to a high and constant food flux. Axis 2 is interpreted as possibly linked to oxygen, but since the conditions never become critical in terms of O_2 concentrations, its role remains largely irrelevant in the composition of benthic foraminiferal assemblages.

5.2. Impact of zonal equatorial dynamics on multiphase biogenic bloom at site U1488

Benthic foraminiferal assemblages at Site U1488 are composed of a few species that show constant high relative abundance (>5 % in more than half of the samples) throughout the studied interval: *Alabaminella weddellensis*, *Epistominella exigua*, *Globocassidulina crassa*, *Globocassidulina subglobosa*, and *Uvigerina proboscidea*. These species display temporary changes in their relative abundance throughout the study interval, which allows for the definition of four intervals and offers insights into the paleoenvironmental changes during the Late Miocene to Early Pliocene at Site U1488.

Interval 1 spans from 8.1 to 6.2 Ma (297.86 to 206.47 m; Fig. 9). The high EBFOI indicates oxic conditions at the seafloor that are further supported by the constant infaunal/epifaunal ratio. This interval is characterised by the high abundance of Subclusters A1 and A2, and it shows the highest percentage of the PET group (e.g., *A. weddellensis*, *E. exigua*, *G. crassa*, and *G. subglobosa*). These species show constant high relative abundance throughout the study interval; however, the highest abundance has been documented between 8.1 and 6.2 Ma. The success of PET within the assemblage relative to other taxa suggests a seasonal input of phytodetritus to the seafloor, related to phytoplankton blooms in surface waters. Species that feed on phytodetritus display an opportunistic behaviour, thriving when seasonal phytodetritus becomes their primary food source (Gooday, 1988, 1993; Suhr et al., 2003; Jorissen et al., 2007). The proliferation of these species is attributed to changes in surface environmental and hydrographic conditions, which result in increased primary productivity and phytoplankton blooms in surface waters, and indicate a high seasonality in the climate regime (Thomas and Gooday, 1996; Jorissen et al., 2007; Corliss et al., 2009).

The high abundance of PET in Interval 1 (the lower part of the study section; Upper Miocene) is tentatively correlated with El Niño-like conditions characterizing the area, with a warm mean state between the western and eastern equatorial Pacific Ocean (Fedorov et al., 2006; Steph et al., 2006; Nathan and Leckie, 2009; Drury et al., 2018). The El Niño-like conditions are related to the Late Miocene sea-level rise, to a relatively unrestricted Indonesian Throughflow (Cane and Molnar, 2001; Molnar and Cane, 2002), and to the weaker trade winds during the Late Miocene due to the reduced latitudinal sea surface temperature gradient and the southward displacement of the Hadley Cell (Herbert et al., 2016; Groeneveld et al., 2017).

At the open-ocean Site U1488, the hypothesised intensification of phytoplankton blooms could be associated with at least two different mechanisms: an increased influx of nutrients to surface waters due to eolian input from the continent, and/or changes in the surface circulation. Modern-day, the enhanced surface primary productivity and related phytoplankton blooms in the equatorial Pacific have been related to increased iron concentrations in surface waters during El Niño phases (Ryan et al., 2002, 2006). Moreover, model simulations show that intensification of the NGCUC during El Niño phases led to erosion of the iron-rich shelf sediments around New Guinea and, in turn, to increased dissolved iron content in the water currents (Ryan et al., 2006).

The upward flux originating from the EUC is thought to be the primary source of iron supply to the euphotic zone in the equatorial Pacific (Coale et al., 1996; Gordon et al., 1997). Alternations in the vertical position of the thermocline and shifts in the EUC have a notable impact on the delivery of iron and macronutrients to the euphotic zone (Mackey et al., 2002). The depth of the thermocline in the equatorial Pacific is controlled by the ENSO, which exerts influence over wind patterns, ocean circulation, and the distribution of water masses within the tropical Pacific zone (Philander, 1989; McPhaden, 1999). The shallowing of the thermocline north of New Guinea during El Niño phases increases the ability of the EUC to collect and transport shelf sediments (Ryan et al., 2006). The anomalously high abundance of PET documented at Site U1488 during Interval 1 may have been triggered by the intensification of the NGCUC (Fig. 1a), as occurs during the modern El Niño-like conditions. This could have led to enhanced iron availability to the WEP, eventually resulting in the intense seasonal phytoplankton blooms observed at Site U1488 during Interval 1.

At the nearby ODP Site 806, between 8.6 and 6.5 Ma, the increase in relative abundance of planktonic foraminiferal genus *Neogloboquadrina*, a taxon related to seasonal productivity, and the reduced δ^{13}C gradient between the upper thermocline and the mixed layer (Nathan and Leckie, 2009), are consistent with the enhanced primary productivity inferred at Site U1488. The siliceous microfossils (i.e., diatoms and radiolarians) at Site U1488 are reported to be abundant in the Upper Miocene sediments until ca. 7.5 Ma, and possibly interpreted as increased productivity in the surface waters over the site (Rosenthal et al., 2018). The increase in $\mathrm{MAR_{Carb}}$ documented at 8.1 Ma is indicative of the onset of the Biogenic Bloom at Site U1488 (Fig. 9). Within Interval 1, the Biogenic Bloom exhibits a fluctuating pattern, characterised initially by a phase of elevated $\mathrm{MAR_{Carb}}$ values spanning from 8.1 to 7.1 Ma, succeeded by a decline between 7.1 and 6.2 Ma. Although this fluctuation might allow a further subdivision of Interval 1, the consistent composition of the benthic foraminiferal assemblage throughout this period prompted us to delineate only one interval with consistent paleoenvironmental significance.

A change in the benthic foraminiferal assemblages is recorded between 6.2 and 5.5 Ma and defines Interval 2 (206.47 to 178.53 m; Fig. 9). At ca. 6.5 Ma and lasting until ca. 5.7 Ma, Drury et al. (2018) proposed a switch from a warm mean state, to an asymmetric state with asymmetrical thermocline and high *E*-W gradient in the equatorial Pacific Ocean, indicating a shift from El Niño-like conditions to La Niña-like conditions. The question remains how this scenario reconciles with our benthic foraminiferal dataset.

The high EBFOI values indicate well-oxygenated bottom waters, and BFARs are high. No major variations in the assemblages have been observed, but we document positive abundance peaks of species that are scarce throughout the rest of the study interval (e.g., *Bulimina marginata*, *Cassidulina laevigata*, *Cibicicidoides bradyi*, *Cibicidoides micrus*, *Ehrenbergina carinata, Nonion* spp.). Subcluster A1 fluctuates but shows an overall decreasing trend, with only a peak around 5.9 Ma. In the Q-mode cluster analysis, samples belonging to Interval 2 are grouped at low values of Axis 2 (Fig. 7).

PET taxa, while still abundant in the assemblages, decline in relative abundance, with *E. exigua* displaying the most pronounced decrease; while the percentage of *G. crassa* remains relatively high. This species has a preference for phytodetritus but could also indicate enhanced influx of organic matter to the seafloor (Suhr and Pond, 2006; Kuhnt et al., 2007). The high abundance of *G. crassa*, together with the positive peaks of eutrophic and suboxic species such as *B. marginata*, *Eh. carinata*, *U. occidentalis*, and genera *Lagena* spp., *Nonion* spp., *Pleurostomella* spp., and *Uvigerina* spp. (Loubere, 1994; Kaiho, 1994, 1999; Fariduddin and Loubere, 1997; Schmiedl et al., 1997; de Rijk et al., 2000), suggest a change in the productivity regime that could be related to the onset of La Niña-like conditions. Since no evidence for low oxygen conditions was found (e.g., dark organic levels, low EBFOI values), we suggest that the increase in abundance of these eutrophic species and of *G. crassa* among the PET could be related to a change in type of food reaching the seafloor, resulting from a decrease in labile phytodetritus and a possible increase in refractory organic matter. The decrease in PET taxa observed in Interval 2 could thus be related to a weakening of the NGCUC due to the shift from El Niño-like to La Niña-like conditions.

El Niño-like conditions return at the beginning of Interval 3, which spans between 5.5 and 4.5 Ma (159.18 to 126.96 m; Fig. 9) (Drury et al., 2018). During this interval, Subcluster B1 dominates, and the diversity and the heterogeneity of the assemblages slightly increase. Subcluster A1 and the PET group are present but show lower relative abundance compared to Interval 1, indicating a weakening of the phytoplankton blooms and/or a decrease in the seasonality of the climate regime. The increase in *Uvigerina* species already started during the upper part of Interval 2, reaches the maximum percentage in Interval 3. High abundance of *Uvigerina*, in particular *U. proboscidea,* is typically associated to high productivity conditions, particularly when seasonality is low and the productivity is consistently high throughout the year (Loubere, 1998; Gupta and Thomas, 1999; Loubere and Fariduddin, 1999). This interval is also marked by an increase in the relative abundance of *N. umbonifera*, a species commonly associated with oligotrophic conditions and cold, carbonate-corrosive, oxygenated deep waters (Gooday, 1994; Gupta, 1997; Loubere and Fariduddin, 1999; Smart et al., 2007). We exclude the influence of $CaCO_3$-corrosive deep waters at Site U1488 since calcareous benthic foraminifera dominate the assemblages throughout the study interval and no other evidence of $CaCO_3$ dissolution has been observed (e.g., test preservation is good and carbonate content is high). A similar increase in *N. umbonifera* has been documented at ODP Site 806 (between 5.4 and 4.4 Ma) and at DSDP Site 586 (between 5.2 and 4.4 Ma), both located in the WEP (Fig. 9; Hermelin, 1989; Resig and Cheong, 1997). The high abundance of *N. umbonifera* in this region could be explained by an expansion of the oxygen-rich LCDW, which would allow the upslope migration of *N. umbonifera*, a species typically found at abyssal depths (Miller and Katz, 1987).

Interval 4 spans from 4.5 to 3.1 Ma (126.96 to 85.02 m, Fig. 9). The decline in the relative abundance of *N. umbonifera* at the base of this interval marks the conclusion of the influence of the high oxygen water current over Site U1488. The interpretation of a slight decrease in bottom-water oxygenation is supported by the lower EBFOI values, and the increase in the infaunal-epifaunal ratio and in the percentage of species related to suboxic conditions, such as *Nonion* spp. and *Uvigerina proboscidea*. The PET group exhibits a lower relative abundance compared to Interval 1, but the presence of these species in the assemblages remains distinct. This is consistent with the conditions observed in other intervals characterised by El Niño-like conditions (Ravelo et al., 2006). As in Interval 3, the relative abundance of *Uvigerina* species, in particular *U. proboscidea*, is high and indicative of consistently high productivity conditions and low seasonality.

Taking into consideration the three intervals influenced by El Niño-like conditions, we infer a shift in the productivity regimes between Interval 1 and Intervals 3 and 4. All three intervals contain abundant PET, but the highest abundance is documented in Interval 1 and indicates marked seasonality, while intervals 3 and 4 point to reduced seasonality and to a more consistent food supply to the seafloor. The steady input of food documented in the Pliocene could be related to increased dust supply through wind transport and/or increased continental weathering. Overall, while the onset of the Biogenic Bloom in the WEP aligns with other regions, it appears that the productivity regimes during the Biogenic Bloom are heavily influenced by the changes in zonal dynamics between El Niño-like to La Niña-like conditions during the Late Miocene and Early Pliocene. These more complex controls on export productivity in the WEP region may contribute to the difference in the termination of the Biogenic Bloom between the WEP and the EEP.

6. Conclusions

In this study, we investigated the Late Miocene-Early Pliocene interval (8.1–3.1 Ma) at IODP Site U1488 to look into the timing and expression of the Biogenic Bloom in the western equatorial Pacific Ocean. We constructed an improved age model based on calcareous nannofossil biostratigraphy, and we calculated the linear sedimentation rates and the MAR_{Carb}. The increase in MAR_{Carb} between 8.1 and 4.0 Ma allows for the identification of the Late Miocene-Early Pliocene Biogenic Bloom, characterised by a fluctuating pattern, and a marked decrease in MAR_{Carb} between 7.1 and 6.2 Ma.

Benthic foraminiferal analyses highlighted Site U1488 experiences four distinct intervals with paleoenvironmental significance. Intervals 1 (8.1–6.2 Ma), 3 (5.5–4.5 Ma), and 4 (4.5–3.1 Ma) are characterised by a high abundance of PET, associated with El Niño-like conditions. This group is abundant in all three intervals, but its highest abundance in Interval 1 indicates elevated seasonality. In contrast, Intervals 3 and 4 suggest a reduction in seasonality and a more consistent food input to the seafloor, possibly linked to increased dust supply through wind transport and/or heightened continental weathering during the Pliocene. Interval 3 is marked by high abundance of *N. umbonifera*, a trend that has also been reported from other sites in the WEP, suggesting an expansion of the oxygen-rich LCDW at a regional scale. Interval 2 (6.2–5.5 Ma) is the only interval spanning La Niña-like conditions, characterised by changes in the type of food reaching the seafloor and/or a decrease in seasonality.

The benthic foraminiferal accumulation rates and inferred export productivity at this site seem to have been mainly influenced by regional processes linked to the El Niño/ La Niña-like conditions, rather than by the Biogenic Bloom per se. The use of the increase in BFAR as a proxy for the Biogenic Bloom should be approached with caution, considering the climatic and oceanographic conditions specific to each site. Nevertheless, the analysis of benthic foraminifera is a valuable tool for investigating paleoenvironmental conditions at the seafloor during the Biogenic Bloom. Ultimately, the benthic assemblage data from Site U1488 reveals that the Biogenic Bloom was not a prolonged phase of high productivity persisting consistently for millions of years, but instead was marked by high variability and different complex productivity phases.

Supplementary data to this article can be found online at https://doi.org/10.1016/j.marmicro.2024.102395.

CRediT authorship contribution statement

Maria Elena Gastaldello: Writing – review & editing, Writing – original draft, Investigation, Data curation, Conceptualization. **Claudia Agnini:** Writing – review & editing, Supervision, Conceptualization. **Thomas Westerhold:** Writing – review & editing, Investigation. **Anna Joy Drury:** Writing – review & editing. **Laia Alegret:** Writing – review & editing, Supervision, Conceptualization.

Declaration of competing interest

At least one of the (co-)authors is a member of the editorial board of Marine Micropalentology. The authors also have no other competing interests to declare.

Claudia Agnini reports financial support was provided by RETURN Extended Partnership, financed by the National Recovery and Resilience Plan–NRRP, Mission 4, Component 2, Investment 1.3–D.D. 1243 2/8/2022, PE0000005. Laia Alegret reports financial support was provided by Spain Ministry of Science and Innovation, MCIN/ AEI/10.13039/501100011033 and by “ERDF A way of making Europe.”, Grant PID2019-105537RB-I00. Maria Elena Gastaldello reports travel was provided by CARIPARO Ph.D. scholarship and by Fondazione Ing. Aldo Gini scholarship. If there are other authors, they declare that they have no known competing financial interests or personal relationships that could have appeared to influence the work reported in this paper.

Data availability

Data generated in this study are available in the Supporting Information and in PANGAEA database (Gastaldello et al., 2024c).

Acknowledgments

This work was funded by University of Padova DOR grant, CARIPARO Ph.D. scholarship, Fondazione Ing. Aldo Gini scholarship, and Grant PID2019-105537RB-I00 funded by MCIN/ AEI/10.13039/501100011033 and by “ERDF A way of making Europe.” C.A. was provided by RETURN Extended Partnership, financed by the National Recovery and Resilience Plan–NRRP, Mission 4, Component 2, Investment 1.3–D.D. 1243 2/8/2022, PE0000005. This research used samples and data provided by the International Ocean Discovery Program (IODP).

References

Agnini, C., Fornaciari, E., Raffi, I., Catanzariti, R., Pälike, H., Backman, J., Rio, D., 2014. Biozonation and biochronology of Paleogene calcareous nannofossils from low and middle latitudes. Newsl. Stratigr. 47 (2), 131–181.

Backman, J., Raffi, I., 1997. Calibration of Miocene nannofossil events to orbitally tuned cyclostratigraphies from Ceara rise. In: Proceedings of the Ocean Drilling Program, Scientific Results, Vol. 154, pp. 83–99.

Backman, J., Shackleton, N.J., 1983. Quantitative biochronology of pliocene and early pleistocene calcareous nannofossils from the Atlantic, Indian and Pacific oceans. Mar. Micropaleontol. 8 (2), 141–170.

Backman, J., Raffi, I., Rio, D., Fornaciari, E., Pälike, H., 2012. Biozonation and biochronology of Miocene through Pleistocene calcareous nannofossils from low and middle latitudes. Newsl. Stratigr. 45 (3), 221–244. https://doi.org/10.1127/0078-0421/2012/0022.

Berger, W.H., Leckie, R.M., Janecek, T.R., Stax, R., Takayama, T., 1993. Neogene carbonate sedimentation on Ontong-Java-Plateau highlights and open questions. In: Proc ODP Sci Res, Vol. 130, pp. 711–744. https://doi.org/10.2973/odp.proc.sr.130.051.1993.

Berggren, W.A., Kent, D.V., Van Couvering, J.A., 1985. In: Snelling, N.J. (Ed.), Geol. Soc. London Mem 10, 211–260.

Bernhard, J.M., 1986. Characteristic assemblages and morphologies of benthic foraminifera from anoxic, organic-rich deposits; Jurassic through Holocene. J. Foraminiferal Res. 16 (3), 207–215. https://doi.org/10.2113/gsjfr.16.3.207.

Bernhard, J.M., Sen Gupta, B.K., 1999. Foraminifera of oxygen-depleted environments. Modern Foramin. 201.

Boscolo-Galazzo, F., Thomas, E., Giusberti, L., 2015. Benthic foraminiferal response to the Middle Eocene climatic optimum (MECO) in the South-Eastern Atlantic (ODP Site 1263). Palaeogeogr. Palaeoclimatol. Palaeoecol. 417, 432–444. https://doi.org/10.1016/j.palaeo.2014.10.004.

Bown, P., Young, J., 1998. Techniques. In: Bown, P.R. (Ed.), Calcareous nannofossil biostratigraphy. Chapman & Hall, pp. 16–28.

Bremer, M.L., Lohmann, G.P., 1982. Evidence for primary control of the distribution of certain Atlantic Ocean benthonic foraminifera by degree of carbonate saturation. Deep Sea Res. Part A Oceanogr. Res. Pap. 29 (8), 987–998.

Cane, M.A., Molnar, P., 2001. Closing of the Indonesian seaway as a precursor to east African aridification around 3–4 million years ago. Nature 411 (6834), 157–162.

Coale, K.H., Fitzwater, S.E., Gordon, R.M., Johnson, K.S., Barber, R.T., 1996. Control of community growth and export production by upwelled iron in the equatorial Pacific Ocean. Nature 379 (6566), 621–624.

Corliss, B.H., 1985. Microhabitats of benthic foraminifera within deep-sea sediments. Nature 314 (6010), 435–438.

Corliss, B.H., 1991. Morphology and microhabitat preferences of benthic foraminifera from the Northwest Atlantic Ocean. Mar. Micropaleontol. 17 (3–4), 195–236. https://doi.org/10.1016/0377-8398(91)90014-W.

Corliss, B.H., Chen, C., 1988. Morphotype patterns of Norwegian Sea deep-sea benthic foraminifera and ecological implications. Geology 16 (8), 716–719. https://doi.org/10.1130/0091-7613.

Corliss, B.H., Brown, C.W., Sun, X., Showers, W.J., 2009. Deep-sea benthic diversity linked to seasonality of pelagic productivity. Deep-Sea Res. I Oceanogr. Res. Pap. 56 (5), 835–841.

Cravatte, S., Kestenare, E., Marin, F., Dutrieux, P., Firing, E., 2017. Subthermocline and intermediate zonal currents in the tropical Pacific Ocean: Paths and vertical structure. J. Phys. Oceanogr. 47 (9), 2305–2324.

de Rijk, S., Jorissen, F.J., Rohling, E.J., Troelstra, S.R., 2000. Organic flux control on bathymetric zonation of Mediterranean benthic foraminifera. Mar. Micropaleontol. 40 (3), 151–166.

Dickens, G.R., Barron, J.A., 1997. A rapidly deposited pennate diatom ooze in Upper Miocene-lower Pliocene sediment beneath the North Pacific polar front. Mar. Micropaleontol. 31 (3–4), 177–182.

Dickens, G.R., Owen, R.M., 1994. Late Miocene-early Pliocene manganese redirection in the central Indian Ocean: Expansion of the intermediate water oxygen minimum zone. Paleoceanography 9 (1), 169–181. https://doi.org/10.1029/93PA02699.

Dickens, G.R., Owen, R.M., 1999. The latest Miocene–early Pliocene BB: a revised Indian Ocean perspective. Mar. Geol. 161 (1), 75–91. https://doi.org/10.1016/S0025-3227(99)00057-2.

Diester-Haass, L., Meyers, P.A., Vidal, L., 2002. The late Miocene onset of high productivity in the Benguela current upwelling system as part of a global pattern. Mar. Geol. 180 (1–4), 87–103.

Diester-Haass, L., Billups, K., Emeis, K.C., 2005. In search of the late Miocene–early Pliocene "biogenic bloom" in the Atlantic Ocean (Ocean ng Program Sites 982, 925, and 1088). Paleoceanography 20 (4). https://doi.org/10.1029/2005PA001139.

Drury, A.J., Lee, G.P., Gray, W.R., Lyle, M., Westerhold, T., Shevenell, A.E., John, C.M., 2018. Deciphering the state of the late Miocene to early Pliocene equatorial Pacific. Paleoceanogr. Paleoclimatol. 33 (3), 246–263.

Drury, A.J., Kulhanek, D.K., Westerhold, T., Ravelo, A.C., Mountain, G., Holbourn, A., et al., 2021. Data report: composite depth scale and splice revision for IODP Site U1488 (Expedition 363 Western Pacific warm Pool) using XRF core scanning data and core images. Proc. Int. Ocean Discov. Prog. 363.

Fariduddin, M., Loubere, P., 1997. The surface ocean productivity response of deeper water benthic foraminifera in the Atlantic Ocean. Mar. Micropaleontol. 32 (3–4), 289–310.

Farinacci, A., Howe, R.W., 1969–2022. The Farinacci and Howe Catalog of Calcareous Nannofossils, 1-26.

Farrell, J.W., Raffi, I., Janecek, T.R., Murray, D.W., Levitan, M., Dadey, K.A., et al., 1995. 35. Late Neogene sedimentation patterns in the eastern equatorial Pacific Ocean. In: Proceedings of the Ocean Drilling Program, Scientific Results, 138, pp. 2419–2426.

Faucher, G., Riebesell, U., Bach, L.T., 2020. Can morphological features of coccolithophores serve as a reliable proxy to reconstruct environmental conditions of the past? Clim. Past 16 (3), 1007–1025.

Fedorov, A.V., Dekens, P.S., McCarthy, M., Ravelo, A.C., DeMenocal, P.B., Barreiro, M., et al., 2006. The Pliocene paradox (mechanisms for a permanent El Niño). Science 312 (5779), 1485–1489.

Filippelli, G.M., 1997. Intensification of the Asian monsoon and a chemical weathering event in the late Miocene–early Pliocene: implications for late Neogene climate change. Geology 25 (1), 27–30.

Fine, R.A., Lukas, R., Bingham, F.M., Warner, M.J., Gammon, R.H., 1994. The western equatorial Pacific: a water mass crossroads. J. Geophys. Res. Oceans 99 (C12), 25063–25080.

Firing, E., 1987. Deep zonal currents in the central equatorial Pacific. J. Mar. Res. 45 (4), 791–812.

Fisher, R.A., Corbet, A.S., Williams, C.B., 1943. The relation between the number of species and the number of individuals in a random sample of an animal population. J. Anim. Ecol. 12, 42.

Fontanier, C., Jorissen, F.J., Licari, L., Alexandre, A., Anschutz, P., Carbonel, P., 2002. Live benthic foraminiferal faunas from the Bay of Biscay: faunal density, composition, and microhabitats. Deep-Sea Res. I Oceanogr. Res. Pap. 49 (4), 751–785. https://doi.org/10.1016/S0967-0637(01)00078-4.

Gasperi, J.T., Kennett, J.P., 1993. Vertical thermal structure evolution of Miocene surface waters: western equatorial Pacific DSDP Site 289. Mar. Micropaleontol. 22 (3), 235–254.

Gastaldello, M.E., Agnini, C., Westerhold, T., Drury, A.J., Sutherland, R., Drake, M.K., et al., 2023. The late Miocene-early Pliocene Biogenic Bloom: an integrated study in the Tasman Sea. Paleoceanogr. Paleoclimatol., e2022PA004565 https://doi.org/10.1029/2022PA004565.

Gastaldello, M. E., Agnini, C., Alegret, L. (2024a). Late miocene to early pliocene benthic foraminifera from the Tasman Sea (International Ocean Discovery Program Site U1506), J. Micropalaeontol., 43, 1–35. doi: https://doi.org/10.5194/jm-43-1-2024, 2024.

Gastaldello, M.E., Agnini, C., Westerhold, T., Drury, A.J., Alegret, L., 2024b. A benthic foraminifera perspective of the late miocene-early pliocene biogenic bloom at ODP Site 1085 (Southeast Atlantic Ocean). Palaeogeogr. Palaeoclimatol. Palaeoecol. 638, 112040 https://doi.org/10.1016/j.palaeo.2024.112040.

Gastaldello, M.E., Agnini, C., Westerhold, T., Drury, A.J., Alegret, L., 2024c. Age Model, Carbonate Mass Accumulation Rates and Benthic Foraminifera From IODP Site 363-U1488 [Dataset Bundled Publication]. PANGAEA. https://doi.org/10.1594/PANGAEA.971539.

Gooday, A.J., 1988. A response by benthic foraminifera to the deposition of phytodetritus in the deep sea. Nature 332 (6159), 70–73. https://doi.org/10.1038/332070a0.

Gooday, A.J., 1993. Deep-sea benthic foraminiferal species which exploit phytodetritus: characteristic features and controls on distribution. Mar. Micropaleontol. 22 (3), 187–205. https://doi.org/10.1016/0377-8398(93)90043-W.

Gooday, A.J., 1994. The biology of deep-sea foraminifera: a review of some advances and their applications in paleoceanography. Palaios 14–31.

Gordon, R.M., Coale, K.H., Johnson, K.S., 1997. Iron distributions in the equatorial Pacific: Implications for new production. Limnol. Oceanogr. 42 (3), 419–431.

Gouriou, Y., Delcroix, T., Eldin, G., 2006. Upper and intermediate circulation in the western equatorial Pacific Ocean in October 1999 and April 2000. Geophys. Res. Lett. 33 (10).

Grant, K.M., Dickens, G.R., 2002. Coupled productivity and carbon isotope records in the Southwest Pacific Ocean during the late Miocene–early Pliocene BB. Palaeogeogr. Palaeoclimatol. Palaeoecol. 187 (1–2), 61–82. https://doi.org/10.1016/S0031-0182(02)00508-4.

Groeneveld, J., Henderiks, J., Renema, W., McHugh, C.M., De Vleeschouwer, D., Christensen, B.A., et al., 2017. Australian shelf sediments reveal shifts in Miocene Southern Hemisphere westerlies. Sci. Adv. 3 (5), e1602567.

Gupta, A.K., 1997. Paleoceanographic and paleoclimatic history of the Somali Basin during the Pliocene-Pleistocene; multivariate analyses of benthic foraminifera from DSDP Site 241 (Leg 25). J. Foraminiferal Res. 27 (3), 196–208.

Gupta, A.K., Thomas, E., 1999. Latest Miocene-Pleistocene productivity and deep-sea ventilation in the Northwestern Indian Ocean (Deep Sea Drilling Project Site 219). Paleoceanography 14 (1), 62–73.

Hammer, Ø., Harper, D., 2005. Paleontological Data Analysis, Oxford. Blackwell Publishing.

Hammer, Ø., Harper, D.A.T., Ryan, P.D., 2001. PAST: paleontological statistics software package for education and data analysis. Paleontol. Electron. 4 (1), 9. https://palaeo-electronica.org/2001_1/past/issue1_01.htm.

Hayward, B.W., Buzas, M.A., 1979. Taxonomy and Paleoecology of Early Miocene Benthic Foraminifera of Northern New Zealand and the North Tasman Sea. https://doi.org/10.5479/si.00810266.36.1.

Hayward, B.W., Sabaa, A., Grenfell, H.R., 2004. Benthic foraminifera and the late quaternary (last 150 ka) paleoceanographic and sedimentary history of the Bounty Trough, east of New Zealand. Palaeogeogr. Palaeoclimatol. Palaeoecol. 211 (1–2), 59–93.

Hayward, B.W., Grenfell, H.R., Sabaa, A.T., Neil, H.L., Buzas, M.A., 2010. Recent New Zealand deep-water benthic foraminifera: taxonomy, ecologic distribution, biogeography and use in paleoenvironmental assessment. GNS Sci. Monogr. 26, 363 (Lower Hutt New Zealand).

Hayward, B.W., Sabaa, A.T., Grenfell, H.R., Neil, H., Bostock, H., 2013. Ecological distribution of recent deep-water foraminifera around New Zealand. J. Foraminiferal Res. 43 (4), 415–442. https://doi.org/10.2113/gsjfr.43.4.415.

Herbert, T.D., Lawrence, K.T., Tzanova, A., Peterson, L.C., Caballero-Gill, R., Kelly, C.S., 2016. Late Miocene global cooling and the rise of modern ecosystems. Nat. Geosci. 9 (11), 843–847. https://doi.org/10.1038/ngeo2813.

Herguera, J.C., Berger, W., 1991. Paleoproductivity from benthic foraminifera abundance: glacial to postglacial change in the West-Equatorial Pacific. Geology 19 (12), 1173–1176.

Hermelin, J.O.R., 1989. Pliocene benthic foraminifera from the Ontong-Java plateau (western equatorial Pacific Ocean): faunal response to changing paleoenvironments. Cushman Found. Foraminiferal Res. Spec. Publ. 26, 1–143.

Hermoyian, C.S., Owen, R.M., 2001. Late miocene-early Pliocene BB: evidence from low-productivity regions of the Indian and Atlantic Oceans. Paleoceanography 16 (1), 95–100. https://doi.org/10.1029/2000PA000501.

Holbourn, A., Henderson, A.S., MacLeod, N., 2013. Atlas of Benthic Foraminifera. John Wiley and Sons. https://doi.org/10.1002/9781118452493.

Hu, D., Wu, L., Cai, W., Gupta, A.S., Ganachaud, A., Qiu, B., et al., 2015. Pacific western boundary currents and their roles in climate. Nature 522 (7556), 299–308.

Johnson, G.C., 2008. Quantifying Antarctic bottom water and North Atlantic deep water volumes. J. Geophys. Res. Oceans 113 (C5).

Johnson, G.C., Sloyan, B.M., Kessler, W.S., McTaggart, K.E., 2002. Direct measurements of upper ocean currents and water properties across the tropical Pacific during the 1990s. Prog. Oceanogr. 52 (1), 31–61.

Jones, R.W., Charnock, M.A., 1985. "Morphogroups" of agglutinated foraminifera. Their life positions and feeding habits and potential applicability in (paleo)ecological studies. Rev. Paléobiol. 4 (2), 311–320.

Jorissen, F.J., de Stigter, H.C., Widmark, J.G., 1995. A conceptual model explaining benthic foraminiferal microhabitats. Mar. Micropaleontol. 26 (1–4), 3–15. https://doi.org/10.1016/0377-8398(95)00047-X.

Jorissen, F.J., Fontanier, C., Thomas, E., 2007. Paleoceanographical Proxies based on Deep-Sea Benthic Foraminiferal Assemblage Characteristics, 1 (07), doi: 10.1016. S1572-5480 (07), 01012-3.

Kaiho, K., 1991. Global changes of Paleogene aerobic/anaerobic benthic foraminifera and deep-sea circulation. Palaeogeogr. Palaeoclimatol. Palaeoecol. 83 (1–3), 65–85.

Kaiho, K., 1994. Benthic foraminiferal dissolved-oxygen index and dissolved-oxygen levels in the modern ocean. Geology 22 (8), 719–722.

Kaiho, K., 1999. Effect of organic carbon flux and dissolved oxygen on the benthic foraminiferal oxygen index (BFOI). Mar. Micropaleontol. 37 (1), 67–76.

Kaminski, M.A., Gradstein, F.M., 2005. Atlas of Paleogene Cosmopolitan Deep-Water Agglutinated Foraminifera, Vol. 10. Grzybowski Foundation.

Kaneko, I., Takatsuki, Y., Kamiya, H., Kawae, S., 1998. Water property and current distributions along the WHP-P9 section (137°–142°) in the western North Pacific. J. Geophys. Res. Oceans 103 (C6), 12959–12984.

Karatsolis, B.T., Lougheed, B.C., De Vleeschouwer, D., Henderiks, J., 2022. Abrupt conclusion of the late Miocene-early Pliocene BB at 4.6-4.4 Ma. Nat. Commun. 13 (1), 1–9.

Kawabe, M., Fujio, S., 2010. Pacific Ocean circulation based on observation. J. Oceanogr. 66, 389–403.

Kawabe, M., Fujio, S., Yanagimoto, D., 2003. Deep-water circulation at low latitudes in the western North Pacific. Deep-Sea Res. I Oceanogr. Res. Pap. 50 (5), 631–656.

Kennett, J.P., von der Borch, C.C., Baker, P.A., Barton, C.E., Boersma, A., Caulet, J.P., et al., 1986. Site 586; western Equatorial Pacific. Initial Rep. Deep Sea Drill. Proj. 90, 19–114. https://doi.org/10.2973/dsdp.proc.90.102.1986.

Kranner, M., Harzhauser, M., Beer, C., Auer, G., Piller, W.E., 2022. Calculating dissolved marine oxygen values based on an enhanced Benthic Foraminifera Oxygen Index. Sci. Rep. 12 (1), 1376.

Kuhnt, T., Schmiedl, G., Ehrmann, W., Hamann, Y., Hemleben, C., 2007. Deep-sea ecosystem variability of the Aegean Sea during the past 22 kyr as revealed by Benthic Foraminifera. Mar. Micropaleontol. 64 (3–4), 141–162.

Lacan, F., Jeandel, C., 2001. Tracing Papua New Guinea imprint on the central Equatorial Pacific Ocean using neodymium isotopic compositions and rare Earth Element patterns. Earth Planet. Sci. Lett. 186 (3–4), 497–512.

Loubere, P., 1994. Quantitative estimation of surface ocean productivity and bottom water oxygen concentration using benthic foraminifera. Paleoceanography 9 (5), 723–737.

Loubere, P., 1998. The impact of seasonality on the benthos as reflected in the assemblages of deep-sea foraminifera. Deep-Sea Res. I Oceanogr. Res. Pap. 45 (2–3), 409–432.

Loubere, P., Fariduddin, M., 1999. Quantitative estimation of global patterns of surface ocean biological productivity and its seasonal variation on timescales from centuries to millennia. Glob. Biogeochem. Cycles 13 (1), 115–133.

Lyle, M., Baldauf, J., 2015. Biogenic sediment regimes in the Neogene equatorial Pacific, IODP Site U1338: Burial, production, and diatom community. Palaeogeogr. Palaeoclimatol. Palaeoecol. 433, 106–128.

Lyle, M., Drury, A.J., Tian, J., Wilkens, R., Westerhold, T., 2019. Late Miocene to Holocene high-resolution eastern equatorial Pacific carbonate records: stratigraphy linked by dissolution and paleoproductivity. Clim. Past 15 (5), 1715–1739.

Mackensen, A., Schmiedl, G., Harloff, J., Giese, M., 1995. Deep-sea foraminifera in the South Atlantic Ocean: ecology and assemblage generation. Micropaleontology 342–358.

Mackey, D.J., O'Sullivan, J.O., Watson, R.J., 2002. Iron in the western Pacific: a riverine or hydrothermal source for iron in the Equatorial Undercurrent? Deep-Sea Res. I Oceanogr. Res. Pap. 49 (5), 877–893.

Marin, F., Kestenare, E., Delcroix, T., Durand, F., Cravatte, S., Eldin, G., Bourdalle-Badie, R., 2010. Annual reversal of the equatorial intermediate current in the Pacific: observations and model diagnostics. J. Phys. Oceanogr. 40 (5), 915–933.

Marino, M., Flores, J.A., 2002. Middle Eocene to early Oligocene calcareous nannofossil stratigraphy at Leg 177 Site 1090. Mar. Micropaleontol. 45 (3–4), 383–398.

Martini, E., 1971. Standard Tertiary and Quaternary calcareous nannoplankton zonation. Proc. II Planktonic Conf. Roma 739–785.

McPhaden, M.J., 1999. Genesis and evolution of the 1997-98 El Niño. Science 283 (5404), 950–954.

Mikkelsen, N., 1990. Cenozoic diatom biostratigraphy and paleoceanography of the western equatorial Indian Ocean. In: Proc. ODP, Sci. Results, 115, pp. 411–432.

Miller, K.G., Katz, M.E., 1987. Eocene Benthic Foraminiferal Biofacies of the New Jersey Transect.

Molnar, P., Cane, M.A., 2002. El Niño's tropical climate and teleconnections as a blueprint for pre-Ice Age climates. Paleoceanography 17 (2), 11-1–11-11.

Murray, J.W., 1988. Neogene bottom water-masses and benthic foraminifera in the NE Atlantic Ocean. J. Geol. Soc. Lond. 145 (1), 125–132.

Murray, J.W., 1991. Ecology and Paleoecology of Benthic Foraminifera. Longman.

Nathan, S.A., Leckie, R.M., 2009. Early history of the Western Pacific warm Pool during the middle to late Miocene (∼ 13.2–5.8 Ma): Role of sea-level change and implications for equatorial circulation. Palaeogeogr. Palaeoclimatol. Palaeoecol. 274 (3–4), 140–159.

Nomura, R., Peirce, J.W., Weissel, J.K., Taylor, E., Dehn, J., Driscoll, N.W., et al., 1991. Oligocene to pleistocene benthic foraminifer assemblages at sites 754 and 756, Eastern Indian Ocean. In: Proceedings of the Ocean Drilling Program. Scientific Results, 121. Texas A and M University, Ocean Drilling Program, pp. 31–75.

Okada, H., Bukry, D., 1980. Supplementary modification and introduction of code numbers to the low-latitude coccolith biostratigraphic zonation (Bukry, 1973; 1975). Mar. Micropaleontol. 5, 321–325. https://doi.org/10.1016/0377-8398(80)90016-X.

Perch-Nielsen, K., 1985. Cenozoic calcareous nannofossils. In: Bolli, H.M., Saunders, J.B., Perch-Nielsen, K. (Eds.), Plankton Stratigraphy. Cambridge University Press, Cambridge, pp. 427–555.

Peterson, L.C., Murray, D.W., Ehrmann, W.U., Hempel, P., 1992. Cenozoic carbonate accumulation and compensation depth changes in the Indian Ocean. In: Synthesis of Results From Scientific Drilling in the Indian Ocean, 70, pp. 311–333.

Philander, S.G., 1989. El Niño, La Niña, and the southern oscillation. Int. Geophys. Ser. 46, X–289.

Pillot, Q., Suchéras-Marx, B., Sarr, A.C., Bolton, C.T., Donnadieu, Y., 2023. A global reassessment of the spatial and temporal expression of the late Miocene Biogenic Bloom. Paleoceanogr. Paleoclimatol. 38 (3), e2022PA004564.

Raffi, I., Flores, J.A., 1995. Pleistocene through Miocene calcareous nannofossils from eastern equatorial Pacific Ocean (Leg 138). In: Proc. ODP, Sci. Results, 138, pp. 233–286.

Raffi, I., Backman, J., Rio, D., 1998. Evolutionary trends of tropical calcareous nannofossils in the late Neogene. Mar. Micropaleontol. 35 (1–2), 17–41.

Raffi, I., Wade, B.S., Pälike, H., Beu, A.G., Cooper, R., Crundwell, M.P., et al., 2020. The neogene period. In: Geologic time scale 2020. Elsevier, pp. 1141–1215.

Ravelo, A.C., Dekens, P.S., McCarthy, M., 2006. Evidence for El Niño-like conditions during the Pliocene. GSA Today 16 (3), 4.

Reghellin, D., Coxall, H.K., Dickens, G.R., Galeotti, S., Backman, J., 2022. The late Miocene-early Pliocene Biogenic Bloom in the Eastern Equatorial Pacific: New Insights from Integrated Ocean Drilling Program Site U1335. Paleoceanogr. Paleoclimatol. 37 (3), e2021PA004313.

Reid, J.L., 1997. On the total geostrophic circulation of the Pacific Ocean: flow patterns, tracers, and transports. Prog. Oceanogr. 39 (4), 263–352.

Resig, J.M., Cheong, H.K., 1997. Pliocene-Holocene benthic foraminiferal assemblages and water mass history, ODP 806B, western equatorial Pacific. Micropaleontology 419–439.

Rio, D., Fornaciari, E., Raffi, I., 1990. Late oligocene through early pleistocene calcareous nannofossils from western equatorial Indian Ocean (Leg 115). In: Proceedings of the Ocean Drilling Program, Scientific Results, 115. Ocean Drilling Program, College Station, Texas, USA, pp. 175–235.

Rosenthal, Y., Holbourn, A.E., Kulhanek, D.K., Aiello, I.W., Babila, T.L., Bayon, G., et al (2018). Site U1488. Western Pacific warm pool. Proceedings of the International Ocean Discovery Program, 363: College Station, TX (International Ocean Discovery Program). Doi: 10.14379/iodp.proc.363.109.2018.

Ryan, J.P., Polito, P.S., Strutton, P.G., Chavez, F.P., 2002. Unusual large-scale phytoplankton blooms in the equatorial Pacific. Prog. Oceanogr. 55 (3–4), 263–285.

Ryan, J.P., Ueki, I., Chao, Y., Zhang, H., Polito, P.S., Chavez, F.P., 2006. Western Pacific modulation of large phytoplankton blooms in the central and eastern equatorial Pacific. J. Geophys. Res. Biogeosci. 111 (G2).

Savin, S.M., Abel, L., Barrera, E., Hodell, D., Kennett, J.P., Murphy, M., et al., 1985. The evolution of Miocene surface and near-surface marine temperatures: oxygen isotopic evidence. In: Kennett, J.P. (Ed.), The Miocene Ocean: Paleoceanography and Biogeography, pp. 49–82.

Schmiedl, G., Mackensen, A., Müller, P.J., 1997. Recent benthic foraminifera from the eastern South Atlantic Ocean: dependence on food supply and water masses. Mar. Micropaleontol. 32 (3–4), 249–287.

Shackleton, N.J., Baldauf, J.G., Flores, J.A., Iwai, M., Moore, T.C., Raffi, I., Vincent, E., 1995. Biostratigraphic summary for Leg 138. In: Proceedings of the Ocean Drilling Program. Scientific Results, 138. Texas A & M University, Ocean Drilling Program, pp. 517–536.

Siedler, G., Holfort, J., Zenk, W., Müller, T.J., Csernok, T., 2004. Deep-water flow in the Mariana and Caroline Basins. J. Phys. Oceanogr. 34 (3), 566–581.

Smart, C.W., King, S.C., Gooday, A.J., Murray, J.W., Thomas, E., 1994. A benthic foraminiferal proxy of pulsed organic matter paleofluxes. Mar. Micropaleontol. 23 (2), 89–99. https://doi.org/10.1016/0377-8398(94)90002-7.

Smart, C.W., Thomas, E., Ramsay, A.T., 2007. Middle–late Miocene benthic foraminifera in a western equatorial Indian Ocean depth transect: paleoceanographic implications. Palaeogeogr. Palaeoclimatol. Palaeoecol. 247 (3–4), 402–420.

Steph, S., Tiedemann, R., Groeneveld, J., Sturm, A., Nürnberg, D., 2006. Pliocene changes in tropical East Pacific upper ocean stratification: response to tropical gateways?. In: Proceedings of the Ocean Drilling Program: Scientific Results, 202, pp. 1–51.

Suhr, S.B., Pond, D.W., 2006. Antarctic benthic foraminifera facilitate rapid cycling of phytoplankton-derived organic carbon. Deep-Sea Res. II Top. Stud. Oceanogr. 53 (8–10), 895–902.

Suhr, S.B., Pond, D.W., Gooday, A.J., Smith, C.R., 2003. Selective feeding by benthic foraminifera on phytodetritus on the western Antarctic Peninsula shelf: evidence from fatty acid biomarker analysis. Mar. Ecol. Prog. Ser. 262, 153–162.

Sutherland, R., Dickens, G.R., Blum, P., Agnini, C., Alegret, L., Asatryan, G., et al., 2019. Expedition 371 methods. In: Tasman Frontier Subduction Initiation and Paleogene Climate. International Ocean Discovery Program. https://doi.org/10.14379/iodp.proc.371.102.2019.

Thomas, E., Gooday, A.J., 1996. Cenozoic deep-sea benthic foraminifers: tracers for changes in oceanic productivity? Geology 24 (4), 355–358.

Tian, Z., Zhou, C., Xiao, X., Wang, T., Qu, T., Yang, Q., et al., 2021. Water-mass properties and circulation in the deep and abyssal Philippine Sea. J. Geophys. Res. Oceans 126 (6), e2020JC016994.

Toole, J.M., Zou, E., Millard, R.C., 1988. On the circulation of the upper waters in the western equatorial Pacific Ocean. Deep Sea Res. Part A Oceanogr. Res. Pap. 35 (9), 1451–1482.

Tsuchiya, M., 1991. Flow path of the Antarctic intermediate water in the western equatorial South Pacific Ocean. Deep Sea Res. Part A Oceanogr. Res. Pap. 38, S273–S279.

Tsuchiya, M., Lukas, R., Fine, R.A., Firing, E., Lindstrom, E., 1989. Source waters of the Pacific equatorial undercurrent. Prog. Oceanogr. 23 (2), 101–147.

Van Morkhoven, F.P.C.M., Berggren, W.A., Edwards, A.S., Oertli, H.J., 1986. Cenozoic Cosmopolitan Deep-Water Benthic Foraminifera, Pau. Elf Aquitaine.

Young, J., 1990. Size variation of Neogene Reticulofenestra coccoliths from Indian Ocean DSDP cores. J. Micropalaeontol. 9 (1), 71–85.

Zhang, L., Chen, M., Xiang, R., Zhang, L., Lu, J., 2009. Productivity and continental denudation history from the South China Sea since the late Miocene. Mar. Micropaleontol. 72 (1–2), 76–85.